Chapter 12
Applications of Induction Synchrotrons

Ken Takayama

12.1 Typical Accelerator Complex Capable of Employing the Induction Synchrotron Scheme

At present there are no plans to construct a new accelerator complex fully employing the *super-bunch* induction acceleration scheme. However, it appears attractive to retrofit many existing accelerator complexes based on RF technology to the induction synchrotron accelerator technology. It is possible to do so by replacing the RF devices without any changes in major components, such as the magnets, injection/extraction devices, vacuum systems, and beam monitoring instruments. Major laboratories in the world promote unique experimental capabilities using specific hadron accelerator complexes. It is interesting to explore how a delivered beam intensity or luminosity in these accelerator complexes is increased by this replacement and consequential for applications. This replacement appears attractive for the hadron accelerator complexes of Fermi National Accelerator Laboratory (8 GeV-Booster/120 GeV-Main Injector/Tevatron) [1], Brookhaven National Laboratory (1.2 GeV-Booster/28 GeV-AGS/RHIC) [2], and CERN (28-GeVPS/450 GeV-SPS/7 TeV-LHC) [3].

12.2 Hybrid Synchrotrons

We call a *hybrid synchrotron* a synchrotron where charged particles are trapped in RF buckets and accelerated with induction voltage. This is an alternative scheme to the full *induction synchrotron* overviewed in Chap. 11; however, both machines are similar in the context of the functional separation in the longitudinal direction. Advanced features associated with the functional separation described in Chap. 11 are realized in the hybrid synchrotron.

K. Takayama (✉)
High Energy Accelerator Research Organization (KEK), Tsukuba 305-0801, Japan
e-mail: takayama@post.kek.jp

K. Takayama, R.J. Briggs (eds.), *Induction Accelerators*, Particle Acceleration and Detection, DOI 10.1007/978-3-642-13917-8_12,

12.2.1 Quasi-adiabatic Focusing-Free Transition Crossing

The method is classified as one of focusing-free transition crossing techniques, where a proton bunch passes through the transition energy with no longitudinal focusing forces, but its acceleration is assured due to flat step-voltages, which are generated with induction acceleration devices. The bunch deformation with shortening in time and stretching in momentum should disappear unless particles in the bunch are subject to confinement voltages, such as the RF voltages, for a short time period before and after the transition energy.

An adiabatic transition crossing method has been demonstrated [4]. An RF bunch can be stretched in time and compressed in energy spread as desired by adiabatically decreasing the RF voltage. If the adiabatic reduction of the RF voltage is performed for a long time period about the transition energy, then nonadiabatic features should be suppressed. This is called a quasi-adiabatic focusing-free transition crossing. In the hybrid synchrotron, in which particles are confined by an RF voltage and accelerated by an induction step-voltage (see Chap. 11), the confinement voltage can be arbitrarily manipulated as long as the particles do not diffuse beyond the accelerating voltage-pulse length. A strict acceleration voltage is necessary so that the orbit of the reference particle follows the center of vacuum chamber.

Consider a small amplitude synchrotron motion near the transition energy. The temporal evolution of the small phase difference from the synchronous particle, $\Delta\tau$, is described by the differential equation [5],

$$\frac{\mathrm{d}^2\Delta\tau}{\mathrm{d}t^2} - \frac{1}{t}\frac{\mathrm{d}\Delta\tau}{\mathrm{d}t} + \frac{4\pi e\gamma_s' t V_{\mathrm{RF}}}{mc^2\gamma_T^4 T^2}\Delta\tau = 0. \tag{12.1}$$

Here γ_T is the transition energy, T is the revolution period of the synchronous particle, V_{RF} is the RF amplitude, and the time t is measured from the transition crossing ($t = 0$). We assume that γ_s is a linear function of time, i.e,

$$\gamma_s = \gamma_T + \gamma_s' t, \tag{12.2}$$

where $\gamma_s'(\equiv \mathrm{d}\gamma_s/\mathrm{d}t)$ is the acceleration rate to satisfy the following relation

$$mc^2\gamma_s' = \frac{eV_a}{T},$$

where $V_a = \rho C_0 \mathrm{d}B/\mathrm{d}t$ is the voltage gain per turn. The slippage factor η given in Eq. (12.1) linearly changes with time near the transition energy according to

$$\eta = \frac{1}{\gamma_T^2} - \frac{1}{\gamma_s^2} \cong \frac{2\gamma_s'}{\gamma_T^3} t. \tag{12.3}$$

We further assume that the RF amplitude for confinement varies in time as

$$V_{\mathrm{RF}} = \pm V_0 \left| \frac{t}{t_0} \right|, \tag{12.4}$$

for a finite time period of $2t_0$, where $V_0 (= \text{const})$ during the time period. The sign of the voltage is changed at transition crossing to maintain the phase stability. The synchronous particle never experiences this RF voltage because it always has zero phase. Substitution of Eq. (12.4) into Eq. (12.1) gives

$$\frac{\mathrm{d}^2 \Delta\tau}{\mathrm{d}t^2} - \frac{1}{t}\frac{\mathrm{d}\Delta\tau}{\mathrm{d}t} + 4\beta^2 t^2 \Delta\tau = 0, \tag{12.5}$$

with

$$\beta^2 = \frac{\pi e \gamma_s' V_0}{mc^2 \gamma_T^4 T^2 t_0}.$$

The independent solutions of Eq. (12.5) are $tJ_{1/2}(\beta t^2)$ and $tN_{1/2}(\beta t^2)$, where $J_{1/2}(x)$ and $N_{1/2}(x)$ are the Bessel functions of half-integer order [6]. Thus, the general solution of Eq. (12.5) is $c_1 tJ_{1/2}(\beta t^2) + c_2 tN_{1/2}(\beta t^2)$ with coefficients c_1, c_2, which are determined from initial conditions. The Bessel function expressions can be expressed in terms of the elementary functions as

$$\begin{aligned} tJ_{1/2}(\beta t^2) &= t\sqrt{\frac{2}{\pi\beta t^2}}\sin(\beta t^2) = \sqrt{\frac{2}{\pi\beta}}\sin(\beta t^2), \\ tN_{1/2}(\beta t^2) &= -tJ_{-1/2}(\beta t^2) \\ &= -t\sqrt{\frac{2}{\pi\beta t^2}}\cos(\beta t^2) = -\sqrt{\frac{2}{\pi\beta}}\cos(\beta t^2), \end{aligned}$$

Using these results, we obtain

$$\Delta\tau = c_1 tJ_{1/2}(\beta t^2) + c_2 tN_{1/2}(\beta t^2) = c_3\sqrt{\frac{2}{\pi\beta}}\sin(\beta t^2 + \delta). \tag{12.6}$$

In Eq. (12.6), c_3 and δ are determined by the initial condition of an individual particle at $t = -t_0$. Since the amplitude is constant in the time interval $-t_0 < t < t_0$, Eq. (12.6) shows that the maximum excursion in $\Delta\tau$ remains constant during transition crossing, suggesting that the bunch length remains constant. The synchrotron oscillation amplitude, which is subject to adiabatic damping far below the transition energy, is a function of t_0. Thus, one can create a bunch of any length desired and bunch shortening at transition crossing can be avoided.

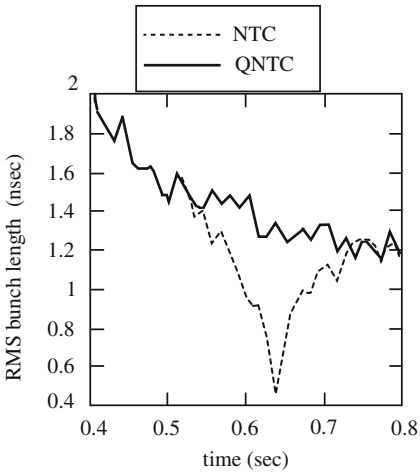

Fig. 12.1 Temporal evolution of the bunch length for two cases (simulations): normal transition crossing (NTC) and qusi-adiabatic focusing-free transition crossing

The feasibility of this method has been extensively studied with computer simulations. Figure 12.1 indicates the temporal evolution near the transition energy, assuming the machine and typical beam parameters of the KEK 12 GeV PS.

The method has been experimentally demonstrated in the hybrid synchrotron. The temporal evolution of the bunch length obtained when the RF voltage amplitude was linearly reduced to zero at the transition energy and then linearly increased according to Eq. (12.4) is shown in Fig. 12.2, together with the case without any RF amplitude reduction. The bunch length behaves as predicted by the simulation. The slight negative slope in time is attributed to adiabatic damping associated with acceleration. It is noted that the RF voltage amplitude reduction starting at time $t = t_0$, at which time the bunch length through the transient region is determined, was arbitrarily chosen. A specific bunch-length desired is obtainable by appropriately choosing t_0.

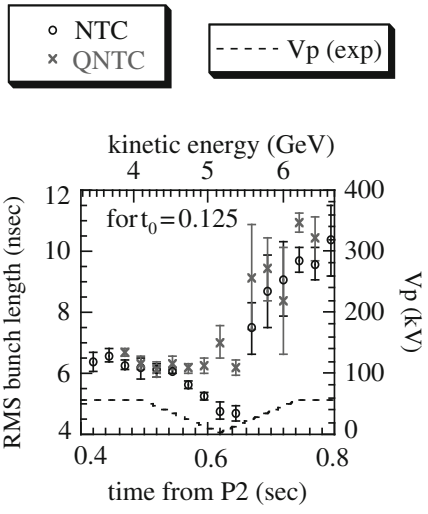

Fig. 12.2 Temporal evolution of the bunch length for two cases (experimental results): normal transition crossing (NTC) and qusi-adiabatic focusing-free transition crossing (QNTC). P2 represents the beginning of acceleration

12.3 Super-Bunch Hadron Colliders

12.3.1 Introduction

A super-bunch hadron collider [7, 8] is a natural application of the induction synchrotron, where super-bunches trapped in the barrier buckets generated with induction step-voltages are collided at collision points. The super-bunch hadron collider promises to increase the luminosity by an order of magnitude because of its capability of accommodating a larger number of particles than a conventional hadron collider based on the RF technology such as LHC [3] and RHIC [2]. This high luminosity is achieved at the expense of risks such as parasitic beam–beam effects and coherent instabilities. On the other hand, crucial beam dynamics issues in the conventional hadron collider such as the e-p instabilities or intra-beam scattering are relaxed. These relaxations result from intrinsic characteristics of the super-bunch and from properties of the collision between super-bunches. In this section we contrast essential aspects of a *super-bunch hadron collider* with a conventional hadron collider. After the proposal of super-bunch hadron colliders, CERN had been exploring a feasibility of the super-bunch scheme in LHC as a possible upgrade path [9]. BNL also is examining the possibility for a super-bunch in the RHIC [10]. In the text, their details including the VLHC [11] with the super-bunch option are described with concrete machine and beam parameters.

12.3.2 Contrast of Coasting Beam, RF Bunch Collider, and Super-Bunch Colliders

A collision between counter-rotating continuous beams has been realized using the CERN Intersecting Storage Rings (ISR) [12] in 1971, which was also the first proton–proton collider. RF bunches were injected from the 28 GeV CERN-PS into the ISR rings and were de-bunched and accelerated up to 31 GeV with a so-called phase-displacement acceleration technique [13] then beams were collided. The ISR experimentally confirmed for the first time that the luminosity of colliders were practically limited by beam–beam interactions, the strength of which were measured by using an incoherent beam–beam tune-shift parameter. Keil et al. carefully investigated the dependence of luminosity and beam–beam tune-shifts in coasting beam colliders on machine/beam parameters and discussed possible ways to maximize the luminosity [14]. Analytical results were refined in [7, 8]. Since the phase-displacement acceleration technique is inefficient, a wide range of acceleration energy is not expected. Thus, a coasting beam collider in a high energy, TeV-class region is unlikely. Indeed, no coasting beam collider has been designed or constructed after the ISR.

The ISR itself was shutdown in a relatively short time. ISABELLE at BNL [15], which was an RF synchrotron and should have provided RF bunches for collision, was designed as a second generation of proton–proton collider and its construction was undertaken in 1978. Although it was switched to a different design

called the Colliding Beam Accelerator (CBA) because of technical problems in the fabrication of superconducting magnets, the project was cancelled in 1983 in favor of a new machine called the Superconducting Super Collider (SSC). Fortunately, the accelerator tunnel constructed for ISABELLE was used for the Relativistic Heavy Ion Collider (RHIC) in 2001. Meanwhile, the construction of SSC began in Texas in 1991 after extensive design work [16] but the project was cancelled in 1993 because of the political decisions induced by increasing cost. The Large Hadron Collider presently being commissioned at CERN is a second proton–proton collider following two unsuccessful US projects. The future Very Large Hadron Collider, which is regarded as a last man-made circular collider, has been studied for design feasibility in US in 2001 [11], but the construction of such a collider is not envisaged within the first quarter of the century.

All hadron colliders mentioned above are RF synchrotrons. Beam bunches in these colliders except the ISR are trapped and accelerated with RF buckets. For the later convenience, we call these colliders a conventional hadron collider (CHC), because they are based on the conventional RF technology. Specific features of a CHC are summarized below: The luminosity is expressed as

$$\mathcal{L} = F\frac{k_b N_b^2 f_{\mathrm{rev}}\gamma}{4\pi\epsilon_n\beta^*}, \tag{12.7}$$

where k_b is the number of bunches per ring, N_b the number of protons per bunch, f_{rev} the revolution frequency, ϵ_n the normalized r.m.s. transverse emittance (assumed to be the same in both planes), β^* the beta-function at the collision point, and $F \leq 1$ is a reduction factor caused by the finite crossing angle Φ.

Although it is clear from the luminosity expression, in which parameters must be improved to increase the luminosity of the CHC, there are limits on the range of beam/machine parameters:

(1) The space-charge limit in the upstream accelerators imposes a limit on the ratio of the number of protons to the emittance, $\Delta\nu \propto N_b/\epsilon_n < 0.25$.
(2) The beam–beam limit, $\xi = \frac{N_b r_0}{4\pi\epsilon_n} \leq 0.004$/Interaction Point ($r_0$, classical radius of proton), which will be discussed in detail in Sect. 12.3.5.
(3) The capability of heat transfer in the cryogenetics of collider magnets gives a synchrotron radiation limit, $P_{\mathrm{rad}}(\propto k_b N_b) \leq\sim$ few watts/m.
(4) Time-resolution of present particle detectors require a minimum bunch spacing something around 5–7 m. Such bunch spacing is created by RF manipulation in the upstream accelerators. In addition, the longitudinal size of each bunch is controlled by using a higher frequency cavity in a downstream accelerator and collider and optimizing the RF voltage to match β^* so as to maximize the luminosity $\mathcal{L}$ for fixed N_b.

The beam occupancy ratio in the entire accelerator circumference, $\kappa = \sqrt{2\pi}k_b\sigma_s/C_0$, typically is limited to 1–3 %.

If the heat deposited by synchrotron radiation on the cryogenic system is removed by engineering solutions and a large number of "pile-up" events is managed by

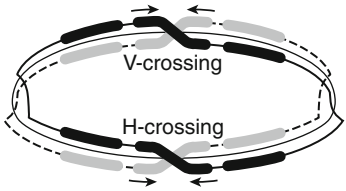

Fig. 12.3 Schematic view of a super-bunch hadron collider

future improvements in particle detectors, then the last factors to determine the ultimate achievable luminosity should be the population of bunch trains along the collider ring and the local density of each bunch. The allowable local density of each bunch depends on specific accelerators within the accelerator complex including the collider. The maximum value for the bunch density in the collider is assumed in the present discussion.

If the proton bunches occupy most of the collider circumference with an allowable momentum spread, the luminosity of hadron colliders can drastically increase. In a typical scheme, 20–30 % of the circumference can be occupied by the proton beam instead of 3–4 %. This situation is essentially like having continuous collisions between proton beams stored in two rings, as seen in Fig. 12.3.

The luminosity for such super-bunch collisions is estimated to be at least 20-times higher than for a CHC. The induction synchrotron discussed in Sect. 11.2.2 is capable of generating a super-bunch, which keeps the same momentum spread and local intensity as in the CHC scheme. After stacking super-bunches in the collider ring and accelerating them with step-voltages generated in the induction gaps to the final energy, multiple super-bunches in both rings are available for collisions. The concept and feasibility of this novel type of collider is reviewed.

12.3.3 Generation of the Super-Bunch

It is not so simple to generate super-bunches for collision in the last-stage collider ring. At the upstream stage of the accelerator complex, a seed for super-bunch must be produced. These super-bunch seeds are merged into a single super-bunch using the barrier-bucket stacking technique described in detail in Sect. 11.2 and illustrated in Fig. 12.4.

As a super-bunch is subject to adiabatic damping associated with acceleration, its bunch length can be reduced by shortening the barrier pulse distance. The momentum spread is determined from the Liouville theorem during this bunch-shortening process. Thus, further stacking of these super-bunches is possible in downstream accelerators. An example of super-bunch handling is shown in Fig. 12.4. In this example, the FNAL accelerator complex is assumed to be the injector of the VLHC. Here, note that a maximum super-bunch length is limited by a practical reason that the induction accelerating pulse-length is order of 1 μs at most, because the longer pulse demands a larger volume of magnetic core material. A barrier-bucket super-bunch seems to be ideal for colliders, because its line density and momentum

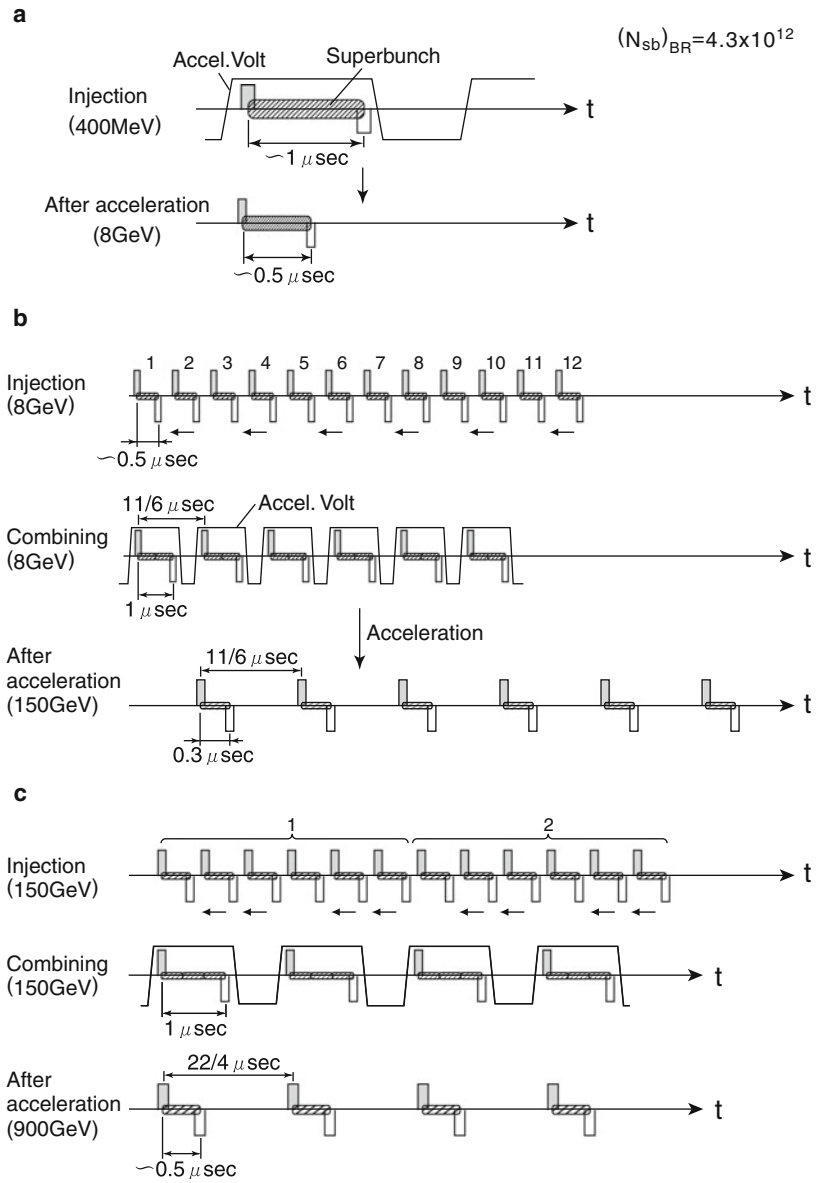

Fig. 12.4 Stacking process in the FNAL accelerator complex as an example of a hadron collider injector. (**a**) LEB (Fermilab BR, $C_o = 474.2$m), (**b**) MEB (Main injector, $C_o = 3.32$ km, $\tau_0 \simeq 11\mu$s), and (**c**) HEB (Tevatron, $C_o = 6.283$ km, $\tau_0 \simeq 22\mu$s)

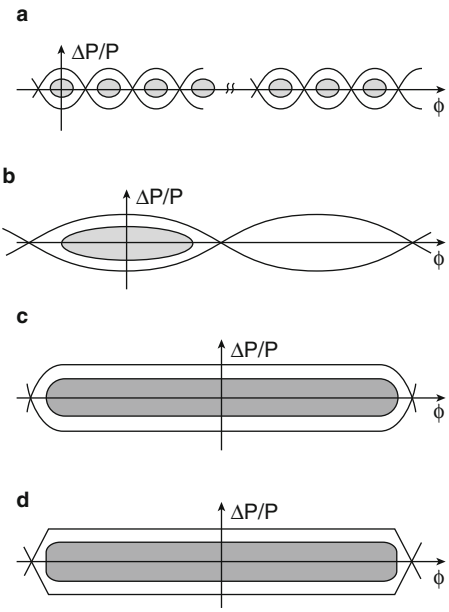

Fig. 12.5 Conventional RF bunches and various types of super-bunch. (**a**) present higher harmonic RF bunch, (**b**) Low harmonic RF super-bunch, (**c**) Super-bunch in an RF barrier bucket, and (**d**) Super-bunch in a step-barrier bucket

spread are almost uniform throughout the bunch. However, there are other types of super-bunch under consideration as shown in Fig. 12.5.

In Table 12.1, a comparison between technological approaches to form super-bunches is made.

Table 12.1 Type of super-bunch

	Low harmonic RF	RF barrier	Step barrier
Technology	Low harmonic cavity low freq. power source	Low Q RF cavity, amplified pulse voltage	Induction cell pulse modulator
Feature			
Advantage	Well-developed, small RF voltage	Already demonstrated, easy bunch formation	Easy bunch formation by controlling trigger timing, uniform line density
Disadvantage	Limited phase-space area, large momentum spread	No acceleration	Beam loading, jitter

12.3.4 Luminosity

The maximum pulse-length of the accelerating induction voltage is typically limited to order of one microsecond due to the practical size of the necessary induction-core. Thus, the collider must be occupied by multiple super-bunches, and bunch

spacing in the ring is used to provide time to reset the magnetic materials. In the case of a VLHC-size ring, the number of super-bunches can be several hundreds (see Sect. 12.3.6). The super-bunch train can occupy a considerable fraction of the ring circumference, typically 20–30%, with a momentum spread determined by the barrier-bucket height. After the beam bunches reach the final energy, a slight accelerating voltage is applied to replenish the energy loss due to synchrotron radiation, while the super-bunches are longitudinally confined with the barrier buckets. Each of the super-bunches intersects with its own counterpart in a half time-period of the bunch length as shown in Fig. 12.3.

Consider a head-on collision between Super-Bunch A and Super-Bunch B. Assuming the super-bunch length ℓ_{sb} is much longer than the effective detector length 2ℓ, an asymmetric feature in collision in the super-bunch head/tail is ignored; a symmetric feature in the core region is taken into account in the following discussion on the luminosity. Super-Bunch A and Super-Bunch B are segmented into pieces of length ds. Particle numbers dN_{A} and dN_{B} contained in a small volume of $dxdyds$ at an arbitrary position (x, y, s) of Super-Bunch A and Super-Bunch B are

$$\begin{aligned} \mathrm{d}N_A &= \rho_A(x, y, s)\mathrm{d}x\mathrm{d}y\mathrm{d}s, \\ \mathrm{d}N_B &= \rho_B(x, y, s)\mathrm{d}x\mathrm{d}y\mathrm{d}s, \end{aligned}$$

where $\rho_A(x, y, s)$ and $\rho_B(x, y, s)$ are the particle number density. A target-size of particles belonging to Super-Bunch B in volume dxdyds is denoted by $\sigma \mathrm{d}N_B$. The probability that a single particle belonging to Super-Bunch A collides with any particle of Super-Bunch B in the small volume dxdyds at the position (x, y, s) is then

$$\sigma \frac{\mathrm{d}N_B}{\mathrm{d}x\mathrm{d}y}.$$

The number of particles of dN_A that collide with any particles in dN_B is

$$\sigma \frac{\mathrm{d}N_B}{\mathrm{d}x\mathrm{d}y}\mathrm{d}N_A.$$

Thus the total number of particles $R(s)$ passing through the entire cross-section at s, which collide with any particles of Super-Bunch B during traversing through ds, is given by the integral

$$R(s) = \sigma \int_{-\infty}^{\infty}\int_{-\infty}^{\infty} \frac{\mathrm{d}N_B}{\mathrm{d}x\mathrm{d}y}\mathrm{d}N_A, = \sigma(\mathrm{d}s)^2 \int_{-\infty}^{\infty}\int_{-\infty}^{\infty} \rho_B(x, y, s)\rho_A(x, y, s)\mathrm{d}x\mathrm{d}y.$$

The total number of particles scattering in the detector region of length 2ℓ is obtained by integrating $R(s)$ from $s = -\ell$ to $s = \ell$,

$$\int_{-\ell}^{\ell} R(s) = \sigma \mathrm{d}s \int_{-\ell}^{\ell} \mathrm{d}s \int_{-\infty}^{\infty}\int_{-\infty}^{\infty} \rho_B(x, y, s)\rho_A(x, y, s)\mathrm{d}x\mathrm{d}y.$$

The total number of particles in Super-Bunch A, which enter into the boundary $s = -\ell$ and collide with any particles in Super-Bunch B at any location within the detector, is then

$$\frac{\ell_{\rm sb}}{{\rm d}s}\int_{-\ell}^{\ell} R(s) = \sigma\ell_{\rm sb}\int_{-\ell}^{\ell}{\rm d}s\int_{-\infty}^{\infty}\int_{-\infty}^{\infty}\rho_B(x,y,s)\rho_A(x,y,s){\rm d}x{\rm d}y,$$

where ℓ_{sb} is the a full length of the super-bunch. Multiplying this result by the bunch revolution frequency in the ring f and the number of super-bunches per ring $k_{\rm sb}$, we have a formula for a total number of proton–proton collisions per second. Dividing it by the cross-section σ, we arrive the luminosity formula,

$$\mathcal{L} = f\ell_{\rm sb}k_{sb}\int_{-\ell}^{\ell}{\rm d}s\int_{-\infty}^{\infty}\int_{-\infty}^{\infty}\rho_A(x,y,s)\rho_B(x,y,s){\rm d}x{\rm d}y. \tag{12.8}$$

Next we consider effects due to the beam crossing in the interaction region with the crossing angle Φ in the (y,s)-plane as illustrated in Fig. 12.6. We introduce primed coordinates related to the x, y, s coordinates by

$$\begin{aligned} x' &= x,\\ y' &= y\cos\Phi + s\sin\Phi \cong y + s\Phi,\\ s' &= s\cos\Phi - y\sin\Phi = s - y\Phi \cong s, \end{aligned}$$

The approximate forms are valid for the usual situation with $\Phi \ll 1$ and $s \gg x, y$.

To first order in the crossing angle Φ, the practical luminosity for one IP (interaction point) is

$$\mathcal{L} = f\ell_{\rm sb}k_{sb}\int_{-\ell}^{\ell} ds\int_{-\infty}^{\infty}\int_{-\infty}^{\infty}\rho_A(x,y,s)\rho_B(x',y',s'){\rm d}x{\rm d}y.$$

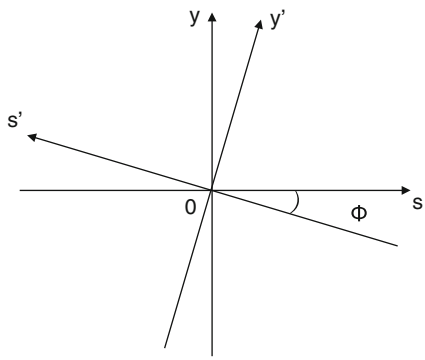

Fig. 12.6 Coordinate system

If the transverse density profile of the super-bunches are assumed to be of Gaussian form with circular cross section, then the particle distribution may be expressed as

$$\rho_A = \frac{\lambda_A}{2\pi\sigma_A^2(s)} \exp\left[-\frac{x^2+y^2}{2\sigma_A^2(s)}\right],$$
$$\rho_B = \frac{\lambda_B}{2\pi\sigma_B^2(s')} \exp\left[-\frac{x'^2+y'^2}{2\sigma_B^2(s')}\right].$$

Here, $\sigma_A = \langle x^2\rangle^{1/2} = \langle y^2\rangle^{1/2}$ is the rms width, and λ_A and λ_B are the constant line densities. The rms beam sizes σ_A^2 and σ_B^2 are related to the beam emittance ϵ and the beta function β by

$$\sigma^2(s) \propto \epsilon\beta(s),$$

where the variation of beta function in the interaction region is described by

$$\beta(s) = \beta^* + \frac{s^2}{\beta^*},$$

with $\beta_x^* = \beta_y^* = \beta^*$. Thus, we obtain

$$\sigma_x(s) = \sigma_y(s) = \sigma^*\left[1+\left(\frac{s}{\beta^*}\right)^2\right]^{1/2},$$

where σ^* is the rms beam size at the crossing point. Evaluating $\mathcal{L}$ in the unprimed coordinate system, we have

$$\begin{aligned}\mathcal{L}_{\mathrm{SHC}}(\Phi, f) &= \frac{f\ell_{\mathrm{sb}}k_{\mathrm{sb}}\lambda_A\lambda_B}{4\pi^2(\sigma^*)^4}\int_{-\ell}^{\ell}\mathrm{d}s\int_{-\infty}^{\infty}\mathrm{d}x\int_{-\infty}^{\infty}\mathrm{d}y\frac{\exp\left\{-\frac{2x^2+y^2+(y+s\Phi)^2}{2(\sigma^*)^2[1+(s/\beta^*)^2]}\right\}}{\left[1+(s/\beta^*)^2\right]^2}\\ &= \frac{f\ell_{\mathrm{sb}}k_{\mathrm{sb}}\lambda^2}{4\pi^2(\sigma^*)^4}\int_{-\ell}^{\ell}\mathrm{d}s\frac{\exp\left\{-\frac{\Phi^2s^2}{2(\sigma^*)^2[1+(s/\beta^*)^2]}\right\}}{1+(s/\beta^*)^2}.\end{aligned} \tag{12.9}$$

Here it is assumed that all super-bunches in the collider have the same line density λ. It is interesting to compare the luminosity $\mathcal{L}_{\mathrm{SHC}}$ in the SHC with $\mathcal{L}_{\mathrm{CHC}}$ in the CHC with the local peak density of λ, using the function of crossing angle Φ' and an effective size (2ℓ) of the particle detector. The luminosity $\mathcal{L}_{\mathrm{CHC}}$, in the CHC, where the transverse particle distribution of an RF bunch is the same Gaussian as that in

the super-bunch and the longitudinal distribution is the Gaussian with the rms length of σ_s, is given by

$$\mathcal{L}_{\rm CHC}(\Phi') = \frac{f k_b (\sigma_s' \lambda)^2}{4(\sigma^*)^2 \sqrt{1 + \left(\frac{\sigma_s \Phi'}{2\sigma^*}\right)^2}},$$

where $\sigma_s' \equiv \sqrt{2\pi}\sigma_s$, and k_b is the number of RF bunches per ring. $\mathcal{L}_{\rm SHC}$ is expressed in term of $\mathcal{L}_{\rm CHC}$ as follows,

$$\mathcal{L}_{\rm SHC}(\Phi, \ell) = 4 \frac{(k_{\rm sb}\ell_{\rm sb})}{(k_b \sigma_s')} \frac{F_{\rm SHC}(\Phi, \ell)}{\sigma_s' F_{\rm CHC}(\Phi')} \mathcal{L}_{\rm CHC}(\Phi'), \tag{12.10}$$

where $F_{\rm CHC}$ and $F_{\rm SHC}$ are the form factors described by

$$F_{\rm CHC}(\Phi') = 1/\sqrt{1 + (\Phi' \sigma_s / 2\sigma^*)^2},$$
$$F_{\rm SHC}(\Phi, \ell) = \int_0^\ell ds \frac{\exp\left(-\frac{\gamma \Phi^2 s^2}{2\beta^* \epsilon_n [1 + (s/\beta^*)^2]}\right)}{[1 + (s/\beta^*)^2]},$$

using $(\sigma^*)^2 = \epsilon_n \beta^* / \gamma$ (ϵ_n: normalized emittance). In the limit of $\Phi = \Phi' = 0$, $k_{\rm sb} = k_b$, $\ell_{\rm sb} = \sigma_s'$, $2\ell = \sigma_s'/2$, Eq. (12.9) becomes $\mathcal{L}_{\rm SHC}(0, \sigma_s'/4) = \mathcal{L}_{\rm CHC}(0)$. The factor of $(k_{\rm sb}\ell_{\rm sb})/(k_b\sigma_s')$ in Eq. (12.10) represents the relative ratio of beam occupation in the SHC/CHC ring circumference. Since $\ell_{\rm sb}$ is determined by engineering limits of super-bunch acceleration as mentioned in Chap. 11, and a total number of particles contained in the super-bunch train, that is, $k_{\rm sb}\ell_{\rm sb}\lambda$ is limited by a level of allowable synchrotron radiation, the relative occupation ratio depends on an available acceleration technology and a collider of concern. For a typical example of the VHC stage-1 design, where

$$\sigma_s' = 15\ {\rm cm}, \quad \beta^* = 0.5\ {\rm m}, \quad \epsilon_n = 1\ \mu{\rm rad},$$
$$\gamma mc^2 = 20\ {\rm TeV}, \quad 2\ell = 5\ {\rm m}, \quad \Phi' = 150\ \mu{\rm rad},$$

and the relative occupation factor of 20 is expected, the normalized luminosity is shown as a function of Φ in Fig. 12.7. Rapid decreasing with the crossing angle is remarkable. This comes from a simple reason that collisions between continuous beams are likely to be affected by the collision angle.

The form factor $F_{\rm SHC}(400\ \mu{\rm rad}, \ell)$ is depicted as a function of ℓ in Fig. 12.8. It shows that the form factor saturates beyond $\ell = 0.1$ m. This suggests that the long-range collision in space between super-bunches does not substantially contribute to the luminosity. Thus, it turns out that the value of beam occupation is crucial to obtain a high luminosity.

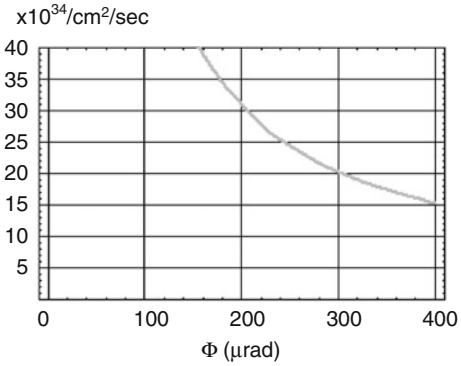

Fig. 12.7 Luminosity versus crossing angle for the VLHC stage-1 parameter

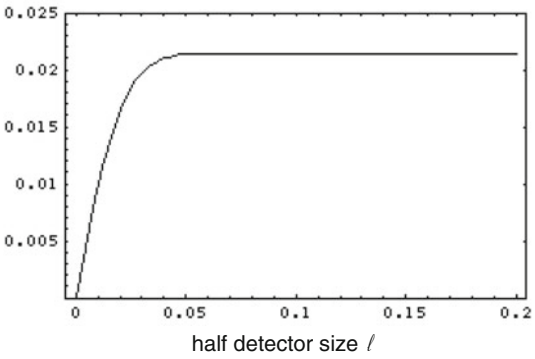

Fig. 12.8 Form factor as a function of ℓ

12.3.5 Beam–Beam Effects and Crossing Geometry

When two super-bunches collide, they exert electromagnetic forces upon each other. The forces are similar to the self space-charge forces on a particle in an intense beam. However, there are two major differences. In the self-induced space-charge force, the characteristic cancellation of electric and magnetic contributions occurs. The self space-charge forces as discussed in Sect. 7.4.1 are given by

$$e(\mathbf{E}+\mathbf{v}\times\mathbf{B}) \cong \left[\mathbf{E}+\mathbf{v}\times\left(\frac{-\mathbf{v}}{c^2}\times\mathbf{E}\right)\right] = e(1-\beta^2)\mathbf{E} \cong \frac{e\mathbf{E}}{\gamma^2}.$$

In the limit of high energy, the force diminishes in importance. In contrast, the magnetic-field generated by the counter-part beam has the opposite sign, because the counter-part beam runs in the opposite direction. Thus, the beam–beam force is proportional to $(1+\beta^2)$. For the high-energy collision $\beta \to 1$, the force approaches the $2e\mathbf{E}$. Both types of space-charge forces are highly nonlinear; the extent of the

nonlinearity depends on the transverse beam distribution. When two beams overlap, the beam–beam force takes a role of defocusing in the transverse direction, yielding a detune in the betatron oscillation frequency. A second major distinction between the two types of forces is that the single-beam space-charge force distributes around the ring circumference with modulation proportional to the envelope function $\beta(s)^{1/2}$; on the other hand, the colliding beams encounter their counter parts at only a few IPs. This suggests that the beam–beam force is quite rich in azimuthal harmonics, contrary to the single-beam space-charge force that is dominated by the 0th harmonic. This feature is important from the beam dynamics point of view, since the non-zero azimuthal harmonics are responsible for the excitation of nonlinear resonances. Even so the 0th harmonic of the beam–beam force, which represents a size of detuning in the betatron oscillation, is important to measure the strength of the beam–beam interaction.

Beyond the interaction region the colliding beams are separated from each other by the deflecting magnets and do not affect each other. Its physical distance $2\ell_{\mathrm{int}}$ is much larger than the effective detector region 2ℓ in a modern high-energy hadron collider.

The beam–beam effects on a particle with non-zero emittance are estimated in a term of non-resonant tune-shift, which represents how much the betatron oscillation frequency is shifted from the machine determined bare-tune by defocusing forces exerting on a particle of concern. Its magnitude is obtained in analytical ways [17, 18] or by numerical methods, once the charge distribution of the counter rotating beam is given. The incoherent tune-shift depends on the oscillation amplitude of the particle and collision geometry, as shown later. In the limit of zero-emittance, the coherent tune-shift is called an incoherent betatron tune-shift, which is related to the first term in an expansion of the beam–beam force with respect to excursion from the center of the betatron oscillation and can be expressed as

$$\Delta\nu_y = \frac{1}{4\pi}\int_0^{C_0} \mathrm{d}s\beta(s)k_y(s),$$

where

$$k_y(s) = \left(\frac{e}{mc^2}\right)\frac{1+\beta^2}{\beta^2\gamma}\left[\frac{\partial E_y}{\partial y}\right]_{y=0}.$$

For the horizontal direction, the expression is the same as the above replacing y by x. This parameter is known to be a good measure of the beam–beam effects.

Incoherent beam–beam tune shift: In the SHC scheme, the incoherent beam–beam tune shift is of big concern as well as coherent beam–beam tune shift, even with a deep crossing angle. The incoherent beam–beam tune-shift can analytically be evaluated by manipulating the non-oscillating terms in the beam–beam

perturbing potential. The tune-shift normalized by that in the head-on collision of the CHC scheme is given in the following forms [7, 8]:

$$\frac{(\Delta\nu_x)_{\Phi}^{\mathrm{SHC}}}{\xi} = \frac{8\beta^*\epsilon_n}{\sigma_s'\gamma}\int_0^{\ell_{\mathrm{int}}} \frac{1+s^2/(\beta^*)^2}{\Phi^2 s^2} \times\left[1-\exp\left(-\frac{\gamma\Phi^2 s^2}{2\epsilon_n\beta^*(1+s^2/(\beta^*)^2)}\right)\right]\mathrm{d}s',$$
$$\frac{(\Delta\nu_y)_{\Phi}^{\mathrm{SHC}}}{\xi} = \frac{8}{\sigma_s'}\int_0^{\ell_{\mathrm{int}}} \exp\left(-\frac{\gamma\Phi^2 s^2}{2\epsilon_n\beta^*(1+s^2/(\beta^*)^2)}\right)\mathrm{d}s - \frac{(\Delta\nu_x)_{\Phi}^{\mathrm{SHC}}}{\xi}, \tag{12.11}$$

Here crossing in the vertical direction is assumed and $2\ell_{\mathrm{int}}$ is the size of the interaction region, $2\ell \ll 2\ell_{\mathrm{int}} \ll \sigma_{\mathrm{sb}}$. In the limit of $\Phi = 0, 2\ell_{\mathrm{int}} = \sigma_s'/2$, Eq. (12.11) become unity. The numerical values for both directions are shown as functions of Φ in Fig. 12.9. A change in the polarity for the vertical direction beyond some critical crossing-angle is notable. This can be understood by recognizing that a particle is focused by space-charge effects as it leaves from the beam-core region, while it is defocused in the core region. Figure 12.10 graphically illustrates this point. Namely, a longer stay outside the core region gives net focusing through the interaction region beyond a certain critical crossing angle. The characteristics strongly suggests that the hybrid crossing (vertical crossing in one interaction region (IR) and horizontal crossing in the other) [7, 8] should be employed in the SHC scheme. The collider rings necessarily have twists. By the hybrid crossing, as schematically shown in Figs. 12.3 and 12.11, the beam–beam tune-shift largely diminishes for both directions. The relative tune-shifts for both directions are less than 2.0 for the crossing-angle beyond 150 μrad, where the luminosity is quite attractive, as found in Fig. 12.7. The magnitude is sufficiently acceptable, because it is equal to the integrated head-on beam–beam tune-shift in the CHC scheme with a couple of IPs.

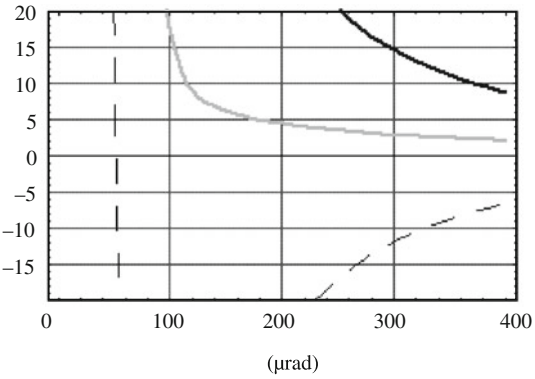

Fig. 12.9 Normalized beam–beam tune shifts for $2\ell_{\mathrm{int}} = 50$ m (*solid*, horizontal; *broken*, vertical; *gray*, sum) for the VHLC stage-1 parameter

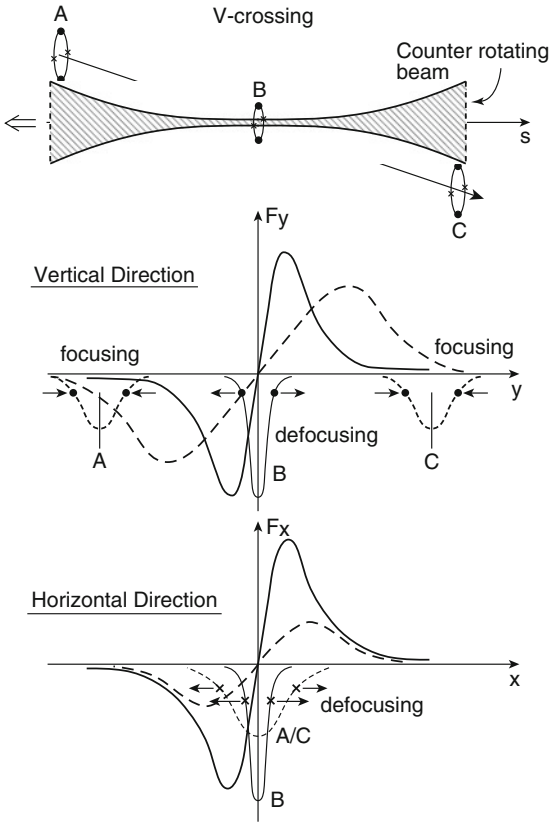

Fig. 12.10 Schematic view of space-charge focusing and defocusing in collision in the s–y plane. *Top*, geometric configuration with a track of a test particle and a change in the beam size of counter rotating super-bunch around the IP; *middle*, the space charge force exerting on the test particle in the vertical direction, where the *broken* and *solid lines* represent the forces at $s = A/C$ and B, respectively; *bottom*, the space charge force exerting on the test particle in the horizontal direction at the same azimuthal locations

Incoherent beam–beam tune-spread and crossing geometry: The beam–beam tune-shift parameters during nominal operations are rather similar to that in the CHC, assuming a same local density. Recent simulations based on the weak–strong model have indicated that an incoherent tune spread due to the continuous parasitic beam–beam interaction is bounded within a tolerable level of 0.015 without any emittance blow-up, assuming the crossing angle of 400 μrad. The full footprint on the tune space is like a bird wing, as shown in Fig. 12.12. This characteristic has been recognized in the earlier work [19]. The tune of large emittance particles locates on the tip of the wing. The footprint for a particle with the smallest emittance in the x-direction and the largest emittance in the y-direction corresponds to the upper tip of wing; meanwhile, the footprint for a particle with the other combination of emittance places on the lower tip. This feature suggests that the footprint on the

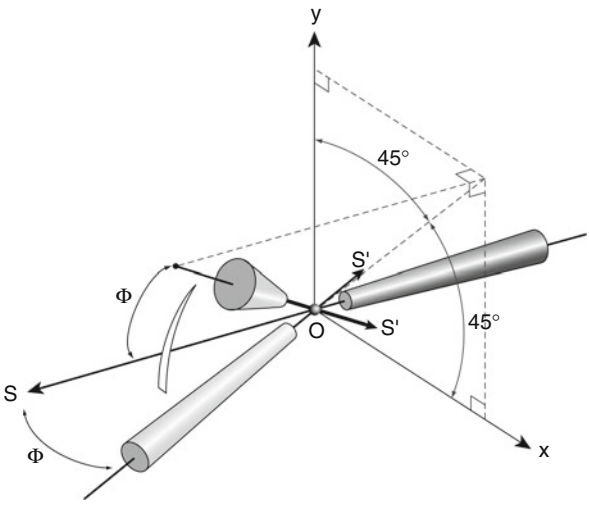

Fig. 12.11 Schematic view of the hybrid crossing and inclined crossing. The super-bunch (*gray*) subject to hybrid crossing has the crossing angle of Φ on the s–x plane; the projection of the s' axis on the x–y plane of the super-bunch subject to inclined hybrid crossing has $\pi/4$ from both axes

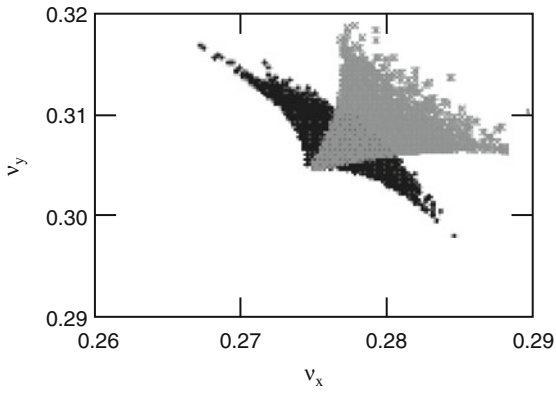

Fig. 12.12 Footprints on the tune space for the hybrid crossing (*black*) and inclined crossing (*gray*). The crossing angle of 400 μrad was assumed and other beam/machine parameters were taken from the LHC

tune space strongly depends on the collision geometry. As a matter of fact, in order to control the tune spread, the inclined crossing in addition to the hybrid crossing, as shown in Fig. 12.11, has been studied. Figure 12.12 denotes that the shape of tune spread is largely modified, substantially reducing a net spread. Details of simulation and its physics background are given in [20–22].

12.3.6 Typical Super-Bunch Collider's Parameters

The typical parameters required on the induction cells employed in the VLHC-size SHC (Superbunch VLHC) are summarized in Table 12.2. RF and beam parameters of the baseline design of VLHC are given in Table 12.3 for comparison. Their operational repetition rate is 431 kHz and the magnitudes of integrated induced voltage for confinement and acceleration are moderate.

Table 12.2 Machine and beam parameters for the LHC

	Unit	CHC	SHC
Storage energy	TeV	7	7
Peak luminosity	$cm^{-2}s^{-1}$	10^{34}	1.5×10^{35}
Number of interaction points		2	2
Circumference	km	26.7	26.7
Revolution freq.	kHz	11.2	11.2
Injection energy	GeV	450	450
Transverse normalized emittance, rms (H & V, flat-top)	μm·rad	3.75	3.75
Initial bunch intensity		1.1×10^{11}	8.77×10^{13}
Number of bunches		2835	46
Total protons/beam		3.12×10^{14}	4×10^{15}
Av.beam current	A	0.56	7.23
Synch. radiation loss/beam	W/m	0.216	2.8
Bunch spacing	μs(m)	0.025(7.48)	1.93(580)
Bunch length rms/full	m	0.075/–	–/150
Beam occupation ratio	%	2	26
Crossing angle	μrad	200	400
β^*	m	0.5	0.5
rms beam size σ^*	m	1.58×10^{-5}	1.58×10^{-5}
Acceleration energy	TeV	6.55	6.55
Acceleration period	s	1,200	1,200
Acceleration voltage/turn	kV	480	480
Induction cell rep-rate	kHz	–	518
Unit induction cell length	m	–	0.2
Unit induction cell voltage	kV	–	2.5
Total No. of A-ICs		–	192
Total length for A-ICs	m	–	38.4
Core-loss of unit cell	kW	–	15
Total core-loss during accel.	MW	–	2.88

On the other hand, a scheme for the RHIC with three super-bunches in each ring, that fill approximately half of the circumference, has been proposed [10]. These super-bunches can be delivered to any experiment, and enough space is provided for the abort gap. Table 12.4 shows the calculated peak luminosities and luminosity lifetimes for the RHIC II and SuperRHIC conditions, where the peak current, limited at the transition energy, is the same in both cases. In addition, the parameters are arranged so that the luminosity lifetime remains constant.

12.3.7 Beam Physics Issues for the Super-Bunch Hadron Collider

12.3.7.1 Head–Tail Instability of a Super-Bunch

A dipole beam breakup mechanism of a super-bunch, called the head–tail instability, is of big concern. As mentioned in Sect. 11.1.2, the synchrotron oscillation frequency of particles trapped in the barrier bucket is small compared to the synchrotron oscillation frequency of particles in the RF bucket. This means that the

Table 12.3 Machine and beam parameters for the VLHC (baseline design)

	Unit	CHC	SHC
Storage energy	TeV	20	20
Peak luminosity	$cm^{-2}s^{-1}$	10^{34}	1.5×10^{35}
Number of interaction points		2	2
Circumference	km	233.037	233.037
Revolution frequency	kHz	1.286	1.286
Injection energy	TeV	0.9	0.9
Transverse normalized emittance, rms (H & V, flat-top)	μm·rad	1.5	1.5
Initial bunch intensity		2.6×10^{10}	5.2×10^{13}
Number of bunches		37152	335
Total protons/beam		9.66×10^{14}	1.74×10^{16}
Av. beam current	A	0.195	3.5
Synch. radiation loss/beam	W/m	0.03	0.538
Bunch spacing	μs(m)	0.019(5.65)	2.32(695)
Bunch length rms/full	m	0.03/–	–/150
Bunch occupation ratio	%	1.2	21.6
Crossing angle	μrad	153	400
β^*	m	0.3	0.3
rms beam size σ^*	m	0.46×10^{-5}	0.46×10^{-5}
Acceleration energy	TeV	19.1	19.1
Acceleration period	s	1000	2,000
Acceleration voltage/turn	MV	14.85	7.425
Energy compensation/turn	keV	38	38
Induction cell rep-rate	kHz	–	431
Unit induction cell length	m	–	0.2
Unit induction cell voltage	kV	–	2.5
Total No. of A-ICs		–	2,970
Total length for A-ICs	m	–	594
Core-loss of unit cell	kW	–	12.5
Total core-loss during acceleration	MW	–	37

Table 12.4 Parameters for heavy ion super-bunch operation in RHIC

	Unit	RHIC II	SuperRHIC
Energy	GeV/au	100	100
Number bunches/beam		111	3
bunch intensity	10^9	1.0	800
Bunch length	m	0.3	600
Averaged beam current	A	0.11	2.4
Crossing angle	μrad	0.0	500
Peak luminisity/IP	$10^{26}cm^{-2}s^{-1}$	70	1,100
number IPs		2	2
Luminosity lifetime	h	3	3

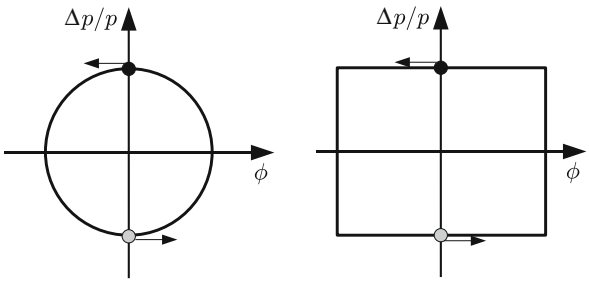

Fig. 12.13 Two macro-particle model. Two particles with the phase difference of π move along the same contour in the longitudinal phase-space for the linear RF-potential (*left*) and the barrier potential (*right*)

interchange between the head and tail particles in the super-bunch doesn't develop quickly, similar to the beam breakup instability in a linac in the limit of $\omega_s = 0$. In order to qualitatively understand the mechanism of the head–tail instability and realize differences between the RF bunch and super-bunch, an elementary model using two *macro-particles* is considered here, each with charge of $Ne/2$, where N is a total number of particles. For simplicity, it is assumed that the synchrotron motion in the RF bucket driving a change between the forward particle and retarded particle is a harmonic oscillation and a particle in the barrier bucket is just reflected at the barriers without time-delay. In addition, the betatron motion to lead to the dipole motion is also assumed to be a harmonic oscillation. In the *two macro-particle model*, an RF bunch or super-bunch consists of two particles, which are located at symmetrical positions on the same contour in the phase-space, as seen in Fig. 12.13. A simple theoretical approach to treat the two macro-particles in an RF synchrotron has been given in the text by A. Chao [23]. This approach is employed here.

Assuming that the wake fields caused by the forwarding particle are simply proportional to its position in the horizontal direction, motions of two particles in a circular accelerator, in which the retarded particle is perturbed by the wake fields, are described by the following equations, for the upper-half time-period of the synchrotron period, $0 < t < \pi/\omega_s$,

$$\begin{aligned} &\mathrm{d}^2x_1/\mathrm{d}t^2 + \omega_1^2 x_1 = 0, \\ &\mathrm{d}^2x_2/\mathrm{d}t^2 + \omega_2^2 x_2 = \left[c^2 N r_0 W_0/(2\gamma C_0)\right] x_1, \end{aligned} \tag{12.12}$$

with

$$\omega_{1,2} = (2\pi c/C_0)\left[\nu_\beta \pm \xi(\Delta p/p) f(t)\right], \tag{12.13}$$

where W_0 is the wake-function integrated over the circumference C_0, r_0 is the classical radius of proton, γ is the relativistic gamma of circulating particle, $\nu_\beta (\omega_\beta = 2\pi c \nu_\beta / C_0)$ is the betatron frequency of an on-momentum particle with $\Delta p/p = 0$ in a normal definition, ξ is the chromaticity, $\Delta p/p$ is the maximum momentum

amplitude, and $f(t)$ is $\cos(\omega_s t)$ for the RF bucket and the step function with amplitude of unity and period of $2\pi/\omega_s$ for the barrier bucket, respectively. Here the particles are assumed to circulate with the speed of light at the first-order approximation. In the lower-half time-period of the synchrotron oscillation, $\pi/\omega_s < t < 2\pi/\omega_s$, the forwarding and retarded particles exchange their roles; the under-suffices in Eq. (12.12) must be replaced with each other. The process is repeated every synchrotron period. The betatron oscillation described by Eq. (12.12) is a harmonic oscillation with the slowly time-varying frequency ($\omega_\beta \gg \omega_s$). Its approximated solution is written in a form of WKB solution,

$$\exp\left[\pm i\int_0^t \omega_{1,2}\mathrm{d}t'\right] = \exp\left[\pm i\left(\frac{\omega_\beta}{\nu_\beta}\right)\left(\nu_\beta t \pm \xi(\Delta p/p)\int_0^t f(t')\mathrm{d}t'\right)\right]. \tag{12.14}$$

Since the Green function is easily expressed in terms of these independent solutions, the non-perturbed and perturbed solutions for Eq. (12.12) are analytically expressed as follows,

$$\begin{aligned} x_1(t) &= c_1 \mathrm{e}^{+i\phi_1(t)} + c_2 \mathrm{e}^{-i\phi_1(t)}, \\ x_2(t) &= c_1' \mathrm{e}^{+i\phi_1(t)} + c_2' \mathrm{e}^{-i\phi_1(t)} + A\int_0^t G(t,t')x_1(t')\mathrm{d}t', \end{aligned}$$

where c_1, c_2, c_1', and c_2' are determined by the initial conditions, and

$$\begin{aligned} A &\equiv \left[c^2 N r_0 W_0/(2\gamma C_0)\right], \\ \phi_{1,2}(t) &= \left(\frac{\omega_\beta}{\nu_\beta}\right)\left(\nu_\beta t \pm \xi(\Delta p/p)\int_0^t f(t')\mathrm{d}t'\right), \\ G(t,t') &= \frac{1}{-2i\omega_{1,2}}\left[-\mathrm{e}^{i(\phi_2(t)-\phi_2(t'))} + \mathrm{e}^{i(\phi_2(t')-\phi_2(t))}\right]. \end{aligned}$$

Here, we introduce a new variable

$$\tilde{x}_{1,2}(t) = x_{1,2}(t) + i\frac{x_{1,2}'(t)}{\omega_{1,2}}. \tag{12.15}$$

Their values at $t = \pi/\omega_s$ are

$$\begin{aligned} \tilde{x}_1(\pi/\omega_s) &= \tilde{x}_1(0)\mathrm{e}^{-i\phi_1(\pi/\omega_s)}, \\ \tilde{x}_2(\pi/\omega_s) &\cong \tilde{x}_2(0)\mathrm{e}^{-i\phi_2(\pi/\omega_s)} \\ &\quad + \frac{iA}{\omega_\beta}\int_0^{\pi/\omega_s} \mathrm{e}^{-i[\phi_2(\pi/\omega_s)-\phi_2(t')]}x_1(t')\mathrm{d}t'. \end{aligned} \tag{12.16}$$

Substituting

$$x_1(t) = \frac{\tilde{x}_1^*(0)}{2}\mathrm{e}^{+i\phi_1(t)} + \frac{\tilde{x}_1(0)}{2}e^{-i\phi_1(t)},$$

into the second term of the right-hand side in Eq. (12.16), we have

$$\tilde{x}_2(\pi/\omega_s) = \mathrm{e}^{-i\phi_2(\pi/\omega_s)}\left(\tilde{x}_2(0) + \left(\frac{A}{2\omega_\beta}\right)\times \right.$$
$$\left\{ \begin{array}{l} \frac{\tilde{x}_1^*(0)}{2\omega_\beta}\left(\mathrm{e}^{+i\frac{2\pi\omega_\beta}{\omega_s}} - 1\right) + \\ \tilde{x}_1(0)\left[\frac{i\pi}{\omega_s} - 2\left(\frac{\omega_\beta}{\nu_\beta}\right)\xi\left(\frac{\Delta p}{p}\right)\int_0^{\pi/\omega_s}\left[\int^{t'} f(t'')\mathrm{d}t''\right]\mathrm{d}t'\right] \end{array} \right\}\Bigg). \tag{12.17}$$

The second term on the right-hand side of Eq. (12.17) is relatively small compared to the third term because of $\omega_\beta \gg \omega_s$. Here it is neglected. The evolution from $t = 0$ to $t = \pi/\omega_s$ is expressed in matrix form as

$$\begin{pmatrix} \tilde{x}_1 \\ \tilde{x}_2 \end{pmatrix}_{t=\pi/\omega_s} \cong \mathrm{e}^{-i\left(\frac{\pi\omega_\beta}{\omega_s}\right)}\begin{pmatrix} 1 & 0 \\ i\Gamma & 1 \end{pmatrix}\begin{pmatrix} \tilde{x}_1 \\ \tilde{x}_2 \end{pmatrix}_{t=0}. \tag{12.18}$$

Here

$$\Gamma \equiv \left(\frac{\pi c^2 N r_0 W_0}{4\gamma C_0 \omega_\beta \omega_s}\right)$$
$$\times\left\{1 + i\frac{2\omega_s}{\pi}\left(\frac{\omega_\beta}{\nu_\beta}\right)\xi\left(\frac{\Delta p}{p}\right)\int_0^{\pi/\omega_s}\left[\int^{t'} f(t'')\mathrm{d}t''\right]\mathrm{d}t'\right\},$$

$$\int_0^{\pi/\omega_s}\left[\int^{t'} f(t'')\mathrm{d}t''\right]\mathrm{d}t' = \begin{cases} 2/\omega_s^2 & \text{in the RF bucket,} \\ \pi^2/2\omega_s^2 & \text{in the barrier bucket,} \end{cases}$$

Beyond $t = \pi/\omega_s$, the forward and retarded particles change their roles. Thus, the change in the parameters after a single period of the synchrotron oscillation is described by

$$\begin{aligned} \begin{pmatrix} \tilde{x}_1 \\ \tilde{x}_2 \end{pmatrix}_{t=2\pi/\omega_s} &\cong \mathrm{e}^{-i\left(\frac{2\pi\omega_\beta}{\omega_s}\right)}\begin{pmatrix} 1 & i\Gamma \\ 0 & 1 \end{pmatrix}\begin{pmatrix} 1 & 0 \\ i\Gamma & 1 \end{pmatrix}\begin{pmatrix} \tilde{x}_1 \\ \tilde{x}_2 \end{pmatrix}_{t=0} \\ &= \mathrm{e}^{-i\left(\frac{2\pi\omega_\beta}{\omega_s}\right)}\begin{pmatrix} 1-\Gamma^2 & i\Gamma \\ i\Gamma & 1 \end{pmatrix}\begin{pmatrix} \tilde{x}_1 \\ \tilde{x}_2 \end{pmatrix}_{t=0}. \end{aligned} \tag{12.19}$$

Since the transfer matrix is known now, stability analysis of this interaction is straightforward. For a weak beam intensity, $|\Gamma| \ll 1$, its eigenvalues are

$$\lambda_{\pm} = \left(1 - \frac{\Gamma^2}{2}\right) \pm i\sqrt{1 - \left(1 - \frac{\Gamma^2}{2}\right)^2} = \mathrm{e}^{\pm i\varphi},$$

where $\sin\frac{\varphi}{2} = \frac{\Gamma}{2}$, and the eigenvectors (+ mode) and (− mode) are

$$U_+ = \begin{pmatrix} -\mathrm{e}^{i\varphi/2} \\ 1 \end{pmatrix}, \quad U_- = \begin{pmatrix} +\mathrm{e}^{-i\varphi/2} \\ 1 \end{pmatrix}.$$

An arbitrary vector at $t = 0$ is expanded in terms of a linear combination of eigenvectors as

$$\begin{aligned} \begin{pmatrix} \tilde{x}_1(0) \\ \tilde{x}_2(0) \end{pmatrix} &= -\frac{\tilde{x}_1(0) - \tilde{x}_2(0)\mathrm{e}^{-i\varphi}}{2\cos\varphi} U_+ + \frac{\tilde{x}_1(0) + \tilde{x}_2(0)\mathrm{e}^{+i\varphi}}{2\cos\varphi} U_- \\ &\approx \frac{1}{2}\left\{-[\tilde{x}_1(0) - \tilde{x}_2(0)]U_+ + [\tilde{x}_1(0) + \tilde{x}_2(0)]U_-\right\}. \end{aligned}$$

It turns out that ± modes represent the distance in the horizontal direction between two particles and the gravity of two particles. The former and latter correspond to motions of the beam size and the bunch center in a real beam, respectively. The imaginary parts of Γ give the growth rate of these modes because of $\phi = \Gamma$,

$$\begin{aligned} (\tau_{\pm})^{-1} &= \mp\frac{\mathrm{Im}(\Gamma)}{2\pi/\Omega_s} \\ &= \mp\left(\frac{c^2 N r_0 W_0}{4\gamma C_0 \nu_\beta}\right) \xi \left(\frac{\Delta p}{p}\right) \omega_s \begin{cases} 2/\pi^2 & \text{in RF bucket,} \\ 1/2 & \text{in barrier bucket.} \end{cases} \end{aligned} \tag{12.20}$$

It is noted that $\Delta p/p$ and ω_s in the barrier bucket or for the super-bunch are not independent. According to Eq. (11.17),

$$\omega_s = \frac{\pi|\eta|(\Delta p/p)}{\Delta t},$$

where $\Delta t\,(< C_0/c)$ is the pulse duration between the barriers and the length of super-bunch in time. In general, ω_s in the barrier bucket is extremely small compared to that in the RF bucket, provided the same magnitude of $\Delta p/p$. Even if a difference in the numerical values on the right-hand side of Eq. (12.20) is considered, therefore, the growth rate in the barrier bucket is much smaller than that in the RF bucket. A beam intensity subjected to the head–tail instability may be estimated from the following relation,

$$N_{\mathrm{super}} = \left(\frac{4}{\pi^2}\right) \frac{(\omega_s)_{\mathrm{RF}}}{(\omega_s)_{\mathrm{barrier}}} N_{\mathrm{RF}}, \tag{12.21}$$

where N_{RF} is the number of particles in a single RF bucket.

The model and theory introduced here is quite simple. It is insufficient to understand various aspects of the head–tail instability in the super-bunch, such as oscillation modes and the instability threshold. Assuming more realistic charge distributions of water-bag and Gaussian, macro-particle simulations have been performed by two groups [24–26]. A fact that the growth rate in the computer simulation [24, 25] decreases with the super-bunch length or Δt is quite consistent to the above prediction. The threshold in the strong head–tail instability regime ($\xi = 0$) has not been observed, while some threshold has been observed for the weak head–tail instability regime [26]. Physics behind these results have not been fully understood yet.

12.3.7.2 Electron-Cloud Effects

Electron-cloud effects are important in super-bunch rings and super-bunch colliders. Electron-cloud effects were first reported in the Proton Storage Ring (PSR) at the Los Alamos National Laboratory [27]. Since then, it has been recognized that it can limit the performance of positron rings and proton–proton colliders. The electron cloud has manifested itself in a variety of ways, such as an increase in vacuum pressure, beam emittance growth and beam loss, degradation of the beam stability, and heating of the vacuum pipe. The electron cloud is known to drive both single and coupled-bunch instabilities, which is known as the e-p instability. Discussion of this instability mechanism is out of the scope of this text; readers are advised to refer to other literature such as [28] for further information. Here we focus our attention only on electron production specific to the super-bunch scheme.

Beam-induced multi-pactoring is believed to be the leading source of sustained electron production. The phenomenon of multi-bunch, beam-induced multipactoring was observed at the CERN PS and SPS [29]. The electron-cloud buildup is known to be sensitive to the intensity, bunch-spacing, and length of the proton bunches, and to the secondary-emission yield of electrons from the vacuum chamber surface. An electron cloud in proton colliders is produced inside the vacuum chamber by a combination of synchrotron radiation, photoemission, secondary emission, and ionization of residual gas, as illustrated in Fig. 12.14.

The major concern in the CHC, where the superconducting magnets are used, is the heat load deposited by the electrons on the beam screen inside the vacuum chamber, which prevents synchrotron radiation from intruding deeply into the superconducting magnets. In LHC, electrons emitted from the wall with an initial energy of less than 10 eV are estimated to acquire a typical energy of 200 eV in the field of a passing bunch. Eventually they transfer this energy to the beam screen. This additional heat load from the electron cloud can be much larger than that due to primary synchrotron radiation, the latter being about 0.2 W/m for the nominal LHC parameters, as mentioned in Sect. 12.3.6. This problem in LHC with a limited cooling capacity has been extensively studied by Zimmermann et al. [9]. They have shown that super-bunches are superior as a remedy against the electron cloud build up and heat load. Most of this subsection is devoted to a summary of these studies.

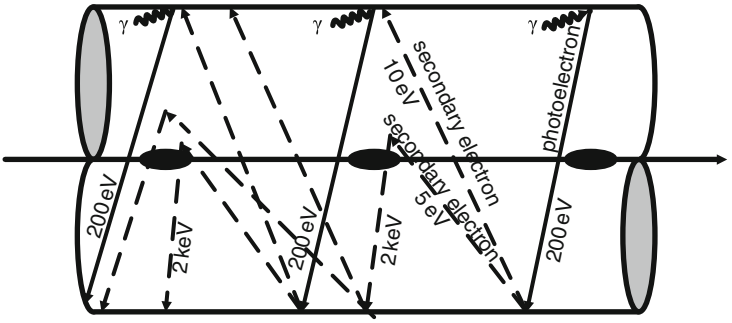

Fig. 12.14 Schematic of electron-cloud build up in the beam pipe during multiple bunch passages, via photo-emission and secondary emission (reproduced from [18] with permission)

In Fig. 12.15 the heat-load curves are given as a function of bunch population N_b for different values of the maximum secondary emission yield for perpendicular incidence, $\delta_{\max}$, which is a critical parameter for the multipacting incidence. The maximum secondary emission yield is known to depend on the surface material and its condition. A cross point of the cooling capacity and the yield in the figure will give an acceptable bunch population. The figure suggests that in order to reach the

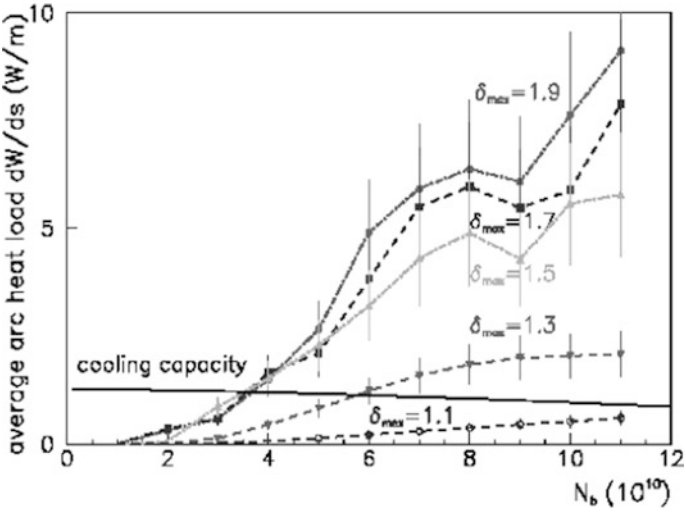

Fig. 12.15 The average LHC arc heat load and cooling capacity versus bunch population N_b, for two values of $\delta_{\max}$; the incident electron energy at the maximum is assumed to be $\epsilon_{\max} = 240$ keV, the photon reflectivity $R = 5\%$ (indicating the fraction of photoelectrons which are emitted uniformly around the chamber azimuth as compared with those on the horizontally outward side), and the photoemission yield per absorbed photon $Y = 5\%$; the elastic reflection of low-energetic electrons on the chamber wall is included. It decreases with bunch population, since at higher current more cooling must be provided for primary synchrotron radiation and image-current heating (reproduced from [9] with permission)

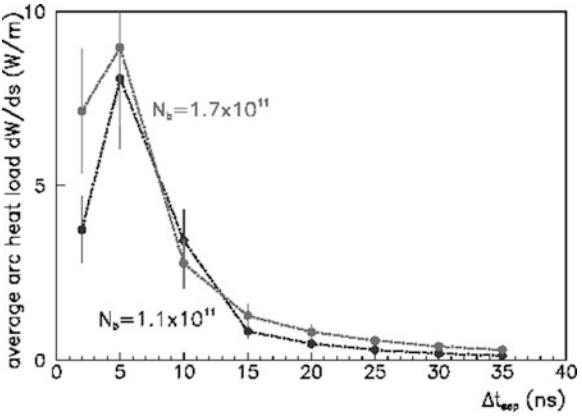

Fig. 12.16 Simulated average LHC arc heat versus bunch spacing, for the maximum secondary emission yield $\delta_{max} = 1.1$ and two bunch populations (reproduced from [18] with permission)

nominal LHC intensity of 1.1×10^{11} per bunch, a secondary emission yield close to 1.1 is required.

Figure 12.16 demonstrates that, even for a secondary emission yield as low as $\delta_{max} = 1.1$, the LHC arc heat load increases to unacceptable levels, if the bunch spacing is reduced below the nominal value of 25 ns. This precludes any luminosity upgrade based on increasing the number of bunches. It is notable, though, that for the shortest spacing 2.5 ns the heat load shows signs of a decrease. It is obvious that the limit of shorter bunch spacing is a coasting beam or a super-bunch. As a matter of fact, the heat load simulation in an LHC arc dipole indicates that its magnitude is remarkably reduced as shown in Fig. 12.17.

A uniform beam corresponds to a static electric potential. In such a potential, electrons emitted from the wall are continuously accelerated towards the centre of

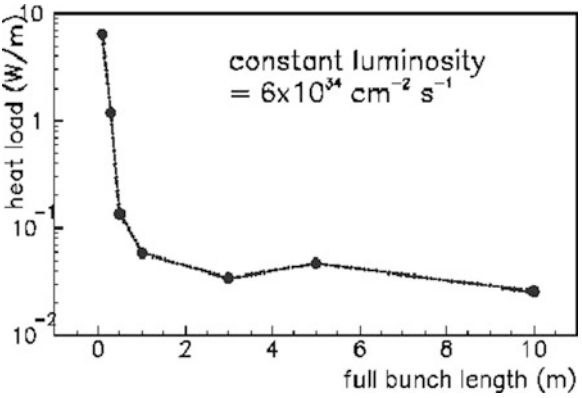

Fig. 12.17 Simulated heat load in an LHC arc dipole due to the electron cloud as a function of super-bunch length for $\delta_{max} = 1.4$, considering a constant flat-top line density of 8×10^{11} m^{-1} with 10% linearly rising and falling edges. The number of bunches is varied so as to keep the luminosity constant and equal to 6×10^{34} cm^{-2}s^{-1} (reproduced from [18] with permission)

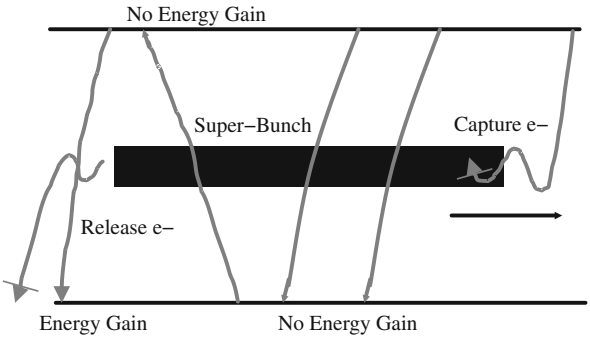

Fig. 12.18 Schematic of electron motion during the passage of a super-bunch. The average energy gain depends on the beam profile. In case of a uniform bunch, electrons do not gain any net energy from the beam, except for those emitted near the bunch tails [30]

the chamber by the electric field of the beam. On the other side of the centre, their kinetic energy decreases again, by the energy conservation law. They impact on the chamber wall with exactly the same energy at which they were emitted. Thus, in the case of a static potential or a uniform beam, no net energy is transferred from the beam to the electrons. This situation is completely different from a beam consisting of separated short bunches, where the potential is time dependent, and the passing bunches give sudden "kicks" to the electrons. The super-bunch mimics the static situation over most of its length. As illustrated in Fig. 12.18, only a small portion of electrons, emitted neat the super-bunch tail, can gain energy during their traversal through the beam. These electrons are responsible for the residual heat load. To keep the number of such electrons low and avoid the so-called "trailing-edge multipactoring", it is important that the beam profile does not decrease near the end of the bunch. If the line density decreases as $\mathrm{d}\lambda/\mathrm{d}t < 0$, the energy gain of an electron at radial position $r(t)$ is roughly described by $\mathrm{d}E/\mathrm{d}t \sim -(\mathrm{d}\lambda/\mathrm{d}t)e^2/(2\pi\epsilon_0)\ln(r(t)/b)$. A flat uniform ($\mathrm{d}\lambda/\mathrm{d}t = 0$) or slightly increasing profile ($\mathrm{d}\lambda/\mathrm{d}t > 0$) followed by a sudden edge is ideal to avoid multipactoring.

12.3.7.3 Intra-beam Scattering

The intra-beam scattering is Coulomb scattering between particles within a bunch. The spatial volume of a beam tends to increase due to the intra-beam scattering. Thus, the luminosity in hadron colliders, which sensitively depends on the spatial volume of colliding beams as understood from Eq. (12.8), is mostly determined due to the intra-beam scattering. The problem was first analyzed by Piwinski [31] and was followed by Bjorken and Mtingwa [32] . Both approaches solve the local, two-particle Coulomb scattering problem for four-dimensional Gaussian for a coasting beam and six-dimensional Gaussian for a bunched beam, assuming non-coupling between three directions. The intra-beam scattering growth-rate for a uniform super-bunch should be similar to that for a coasting beam of equal charge line-density and Gaussian-like energy-spread. Since the microscopic mechanism of intra-beam scattering is common for both cases of bunched beam and coasting beam, the difference originates from averaging over the particle distribution in the longitudinal space. Mathematical formulas useful for a super-bunch trapped in the barrier bucket,

where a pair of steep barrier voltages with an infinitely large amplitude simply repels drifting particles to the opposite direction as depicted in Fig. 11.2, are given here.

Piwinski shows in [33] how the diffusion caused by intra-beam scattering is handled and the diffusion time is derived. Extending Piwinski's result, the rise times for the mean oscillation amplitudes and momentum spread, which determine the super-bunch dimensions, are given by

$$\begin{aligned}
\frac{1}{\tau_p} &= \frac{1}{2\sigma_p^2}\frac{\mathrm{d}\sigma_p^2}{\mathrm{d}t} = A\frac{\sigma_h^2}{\sigma_p^2} f(a,b,c),\\
\frac{1}{\tau_x} &= \frac{1}{2\sigma_x^2}\frac{\mathrm{d}\sigma_x^2}{\mathrm{d}t} = A\left[f\left(\frac{1}{a},\frac{b}{a},\frac{c}{a}\right) + \frac{D^2\sigma_p^2}{\sigma_{x_\beta}^2} f(a,b,c)\right],\\
\frac{1}{\tau_y} &= \frac{1}{2\sigma_y^2}\frac{\mathrm{d}\sigma_y^2}{\mathrm{d}t} = Af\left(\frac{1}{b},\frac{a}{b},\frac{c}{b}\right),
\end{aligned} \tag{12.22}$$

where

$$\begin{aligned}
A &\equiv= \frac{r_p^2 c}{64\pi^2}\frac{2\sqrt{\pi}N}{L}\frac{1}{\sigma_p\sigma_{x_\beta}\sigma_{y_\beta}\sigma_{x'}\sigma_{y'}\beta^3\gamma^4}, \quad \frac{1}{\sigma_h^2} \equiv \frac{1}{\sigma_p^2} + \frac{D^2}{\sigma_{x_\beta}^2},\\
a &\equiv \frac{\sigma_h}{\gamma\sigma_{x'}}, \quad b \equiv \frac{\sigma_h}{\gamma\sigma_{y'}}, \quad c \equiv \beta\sigma_h\sqrt{2\frac{d}{r_p}},\\
f(a,b,c) &= 8\pi\int_0^1 \left\{\ln\left[\frac{c^2}{2}\left(\frac{1}{\sqrt{p}}+\frac{1}{\sqrt{q}}\right)\right] - 0.5777\right\}(1-3x^2)\frac{\mathrm{d}x}{\sqrt{pq}},\\
p &\equiv a^2 + x^2(1-a^2), \quad q \equiv b^2 + x^2(1-b^2),
\end{aligned} \tag{12.23}$$

where r_p is the classical radius, N is the number of particles in the super-bunch, L is the length of the super-bunch, D is the averaged dispersion function, and d is the averaged half beam-height. Note that for a bunched beam $2\sqrt{\pi}N/L$ is replaced by N/σ_s. Equation (12.23) suggests that the rise times never depend on the length of super-bunch if the line density, N/L, is kept constant.

For a collider energy beyond LHC, the synchrotron radiation damping is known to surpass the intra-beam scattering growth rate. The equilibrium emittances will result from a balance of radiation damping, quantum fluctuations, and intra-beam scattering. Its details depend on machine and beam parameters of an individual collider.

12.3.7.4 Other Issue

The so-called Pacman effect [34] has been of concern in hadron colliders since the beginning of SSC design study. Pacman effects in the super-bunch collision have not yet been quantitatively evaluated. However, it is still possible to point out essential

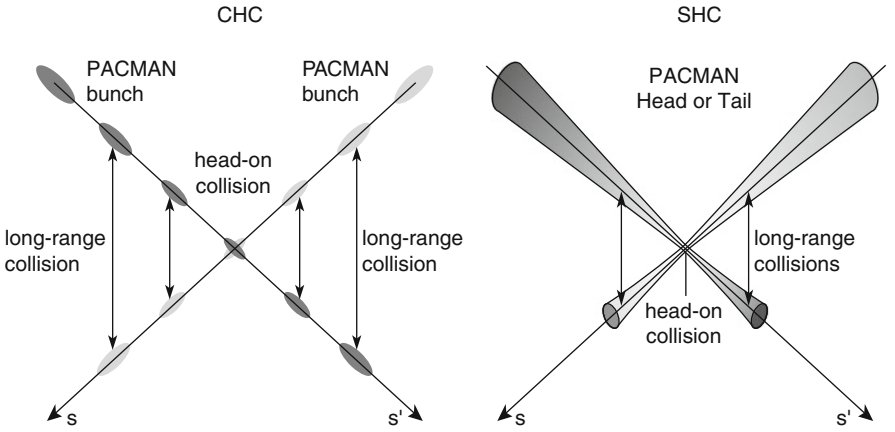

Fig. 12.19 Schematic for Pacman effects. The *left* represents asymmetric collision between the head parts of counter-rotating bunch trains. The *right* represents beginning in the super-bunch collision

differences between the RF bunch collision and super-bunch collision. In the CHC, Pacman bunches, which have no partners to guarantee symmetric collision around the collision point, are isolated in the head and tail regions in the bunch train (see Fig. 12.19). A domino-like vanishing of colliding bunches induced by this asymmetric collision has been of big concern because the blow-up of the Pacman bunches inevitably propagates into the core region of the RF bunch train. Meanwhile, the situation in the super-bunch collision is same with respect to the asymmetry. However, the head and tail of the super-bunch are always mixed in the entire region of the super-bunch due to the synchrotron oscillation. There has been no estimation how this feature can mitigate the Pacman effects.

12.4 All-Ion Accelerator – An Injector-Free Induction Synchrotron

12.4.1 Introduction

For more than 70 years since the original work by Lawrence and Livingston and other researchers in the 1930s [35], the cyclotron has evolved in its various forms. It has become a common choice for the acceleration of a wide variety of different ion species to a medium energy range of multi-hundreds of MeV/au. Any ions that have the same Z/A, where A is the mass number and Z is the charge state, can in principle be accelerated by the same cyclotron. For the acceleration of particular ions far beyond the medium energy region, RF synchrotrons have been used. In the early 1970s, heavy ions, such as N, Xe, and U, were accelerated in the Princeton Particle Accelerator [36] and the Bevatron of Lawrence Berkeley National Laboratory [37].

Those experiments demonstrated the significance of the vacuum pressure in low and medium-energy accelerators, where beam losses due to charge-state changing of partially stripped ions are serious. These days, heavy ions, such as gold and copper, are accelerated in the Alternate Gradient Synchrotron (AGS) and the Relativistic Heavy Ion Collider (RHIC) of Brookhaven National Laboratory to serve for collider experiments [2]. Lead ions are to be accelerated in the Large Hadron Collider (LHC) of CERN for a similar purpose [3]. The heavy-ion medical accelerator of National Institute of Radiological Science in Japan (NIRS) accelerates carbon ions to 400 MeV/au, which are delivered for cancer therapy [38]; in addition, He, N, O, Ne, Si, Ar, and Fe are provided for other purposes, such as radiation-damage tests on biological cells or beam–plasma interactions. The SIS-18 synchrotron [39] of GSI is devoted to material science or warm dense matter science as described in Sect. 10.2.1, providing H, D, C, N, O, Ne, Ar, Ni, Kr, Xe, Au, Bi, and U.

Limit of resonant circular accelerators: The accelerators mentioned above are classified as resonant accelerators employing radio-frequency waves for acceleration. Electric fields varying in time give the required energy per turn and provide the focusing forces in the moving direction. This characteristic in a circular ring has been recognized to be an enormous figure of merit, and is a big reason why the RF acceleration technique has a quite long life-time since its being established. Once the synchrotron is determined to operate on protons, an RF acceleration system consisting of an RF cavity and an RF power-source is fixed. In a typical medium-energy synchrotron, the RF frequency sweeps by one order of magnitude through its entire acceleration associated with increasing the revolution frequency, where the relativistic beta changes from 0.1 to some value close to unity. The kinetic energy of an ion is described by $Amc^2(\gamma - 1)$, where γ is the relativistic gamma of the ion, and m is the proton mass; in the non-relativistic region it is approximated by $(1/2)Amc^2\beta^2$, where β is the relativistic beta. This formula suggests that the injection energy must be above $4.69A$ MeV to meet the RF frequency minimum limit. In other words, the integrated acceleration voltage in an upstream injector must be $V = 4.69(A/Z)$ MeV. So far, this required voltage has been provided by a gigantic static accelerator, such as a Van de Graaff, or by a drift-tube linac. An electro-static accelerator of larger energy than tens of MeV is not practical because of a technical limit of high-voltage breakdown and its huge cost.

Limit of drift tube linacs: A drift tube linac (DTL) is considered as the typical injector for a circular accelerator employing the RF acceleration technology. Ions in the DTL are accelerated in a gap between adjacent electrodes in the so-called π-mode, where electric fields are excited in the opposite direction during the time period when ions propagate in the electrodes. The distance L_i between the center positions of two adjacent i-th and $i + 1$-th electrodes is defined by $L_i = vT/2$, where v is the velocity of ion and T is the RF period at the frequency f. It may be rewritten in the following form

$$L_i = \frac{1}{2f}\sqrt{2\frac{Z}{A}\frac{e}{m}\sum_{j=1}^{i} V_j} \tag{12.24}$$

where V_j is the gap voltage. Once the mechanical geometry of the DTL is fixed, L_i is never changed. In addition, the RF frequency is fixed at the early stage of design. In order to accelerate an arbitrary ion of A and Z, therefore, the acceleration voltage has to be scaled proportionally to A/Z. There are two practical obstacles to the use of the DTL for acceleration of ions with a large A/Z. (1) There is no power source to meet the demand. (2) High voltage operation of the DTL will induce RF breakdown, even if a power source capable of generating the necessary voltage is available. Another possibility is to change the frequency f. Certainly, such a frequency variable DTL exists [40]. Its band is typically changed within a factor of two or three, where it is possible to cover a change in A/Z by a factor of about 5 without increasing the RF voltage. This fact seems to sound good. However, we have to also satisfy the requirement on the ion energy at the end of the DTL. The lower limit of the band-width of the RF synchrotron itself requires a minimum velocity, as mentioned earlier. The velocity of ions injected into the RF synchrotron is described by

$$v = \sqrt{2(Z/A)(e/m)V}, \tag{12.25}$$

Here $V \equiv \sum_{j=1} V_j$ is the integrated acceleration voltage in the DTL. It is apparent that the acceleration voltage has to be changed, depending on A/Z of ions of interest. Thus, it turns out that for the present purpose the RF voltage of the DTL has to be changed. Crucial issues in this case have been already mentioned.

Limit in higher harmonic operation of resonant accelerators: In principle, the acceleration of ions with a velocity far smaller than $\beta = 0.1$ in the RF synchrotron is possible by introducing the harmonic acceleration. The RF frequency, f_{RF}, is kept to be hf_0 ($h \neq 1$) through the entire acceleration, where $f_0 (= C_0/c\beta$, C_0: circumference of the ring) is the revolution frequency. In this higher harmonic acceleration, the accelerated beam is segmented into h pieces of the RF bunch. The harmonic number, h, depends on the initial velocity of the ion, that is, $\sim 1/(10\beta)$. In higher harmonic acceleration, serious beam loss at extraction is inevitable without additional beam handling. Adiabatic recapturing by lower harmonic RF after adiabatic de-bunching is required because RF bunches are uniformly distributed along the entire ring just after acceleration by the higher harmonic RF, and extraction magnets excited in a finite time will kick a substantial fraction of these higher harmonic RF bunches out of the extraction orbit. The additional RF system requires more space in the accelerator ring and the complicated beam-handling is time consuming. Higher harmonic RF acceleration of a low-energy ion beam is not impossible [41], but it is an unattractive option.

Comparison between conventional synchrotron and all-ion accelerator: In Fig. 12.20 above discussions are schematically depicted and a conclusion is arrived at that a simple structure of accelerator complex can be realized. Hereafter, a concept of injector-free synchrotron, which allows the acceleration of all species of ions in a single ring, is described in more detail. In order to overcome the above limits of the existing RF acceleration, a newly developed acceleration technology is employed for the present purpose. Such a synchrotron is called an all-ion accelerator (AIA) [42, 43]; its characteristics and key issues are discussed below.

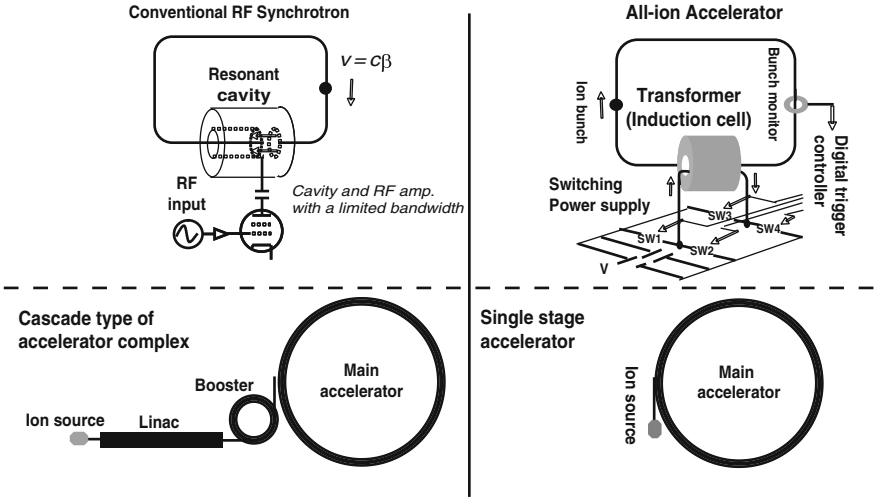

Fig. 12.20 Comparison of essential features of RF synchrotrons and all-ion accelerators based on the induction synchrotron concept

Expected roles of the AIA: So far, the irradiation of various ions on metal, magnetic material, ceramic, semi-conducting material, and polymer has been discussed to develop novel materials, such as nano-wire, nano-transistors, quantum-dots, and conducting ion tracks in diamond-like carbon [44]. Deep implantation of moderate-energy heavy ions may serve to create a new alloy in bulk size. Meanwhile, energy deposition caused by the electro-excitation associated with passing of high-energy ions through the material is known to largely modify its structure [45]. Warm dense matter science is going to drastically evolve with the aid of high-power laser and heavy-ion beams [46]. The irradiation of moderate-energy heavy-ion beams on metal in a small physical space of less than a mm in diameter and in a short time period less than 100 ns is known to create a particularly interesting state of material, where the temperature is 0.1–10 eV and the mass density is 1–10 g/cm^3. This state of matter is far from playing-grounds of solid-state physics and plasma science. Its equation of state has not yet been established, electric conductivity is not known, and the effects of the interactions between atoms are not confirmed.

12.4.2 Concept

Acceleration system of the AIA consists of induction acceleration cell, switching power-supply to drive the cell, the gate signal control system including the bunch monitors, as depicted in Fig. 12.21. A master signal for the gate signal is generated from a circulating ion-bunch signal; thus, induction pulse-voltages for acceleration and confinement are automatically synchronized with the revolution of ion bunch. This property suggests that the allowable revolution frequency is not limited if a

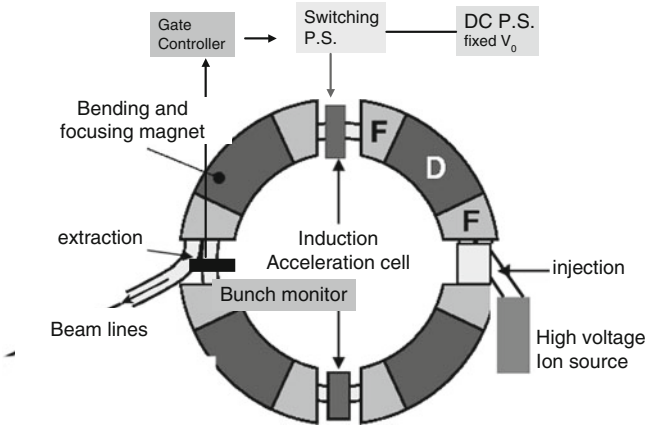

Fig. 12.21 Schematic view of the all-ion accelerator. F and D show the focusing and defocusing part in the combined function magnet, respectively. The ion-bunch signals monitored by the bunch monitor are processed with the gate controller, generating a gate signal for the switching power supply

sufficiently fast switching device is available. This is a big difference from a conventional RF synchrotron or cyclotron, where the range of the acceleration energy or ion mass is limited, since equipped RF devices usually have a finite bandwidth, as mentioned earlier. The AIA is able to accelerate all species of ions of their possible charge state from the lightest to the heaviest. In order to emphasize the unique figure of merits of the AIA, the low energy injection into the AIA is assumed, associated with a wide operational range of magnetic guiding fields. In the following subsections, the essential characteristics of the AIA are discussed, and its typical composition and numerical parameters are given. Taking as an example the KEK 500 MeV Booster Synchrotron, a rapid-cycle proton synchrotron, the beam and machine parameters when modified to an AIA would be:

Circumference	$C_0 = 37$ m
Curvature	$\rho = 3.3$ m
Minimum Field (Ar^{+18})	$B_{\min} = 0.029$ Tesla
Maximum Field (Ar^{+18})	$B_{\max} = 0.8583$ Tesla
Acceleration Voltage (Eq. 12.26)	$V_{\text{acc}} = 6.36$ kV
Machine Cycle	$f = 20$ Hz

12.4.3 Digital Acceleration and Switching Frequency

The acceleration equation for an arbitrary ion with mass $M = Am$ and charge $Q = Ze$, where m and e are the mass of a proton and unit charge, has been evaluated in Sect. 11.4.3. The following relation between the ramped bending field and the

accelerating-voltage have to be satisfied for the orbit of an ion to stay at the center of the accelerator ring:

$$V_{\mathrm{acc}}(t) = \rho C_0 \frac{\mathrm{d}B}{\mathrm{d}t}. \tag{12.26}$$

Equation (12.26) gives the required accelerating voltage, since the ramping pattern of the magnetic field is determined first. There are two typical ramping patterns for $B(t)$:

(1) Excitation by a resonant circuit.
(2) Excitation with a pattern-controlled power supply.

Cases (1) and (2) are typically applied to rapid- and slow-cycling synchrotrons, respectively. Since the former is typical for a medium-energy synchrotron, this case is considered here. $B(t)$ is described

$$\begin{aligned} B(t) &= \frac{1}{2}\left[(B_{\max} + B_{\min}) - (B_{\max} - B_{\min})\cos(\omega t)\right], \\ (\mathrm{d}B/\mathrm{d}t)_{\max} &= \frac{\omega}{2}(B_{\max} - B_{\min}), \end{aligned}$$

where $B_{\min}$ and $B_{\max}$ are the injection field and the extraction field, respectively, and ω is the ramping cycle. From Eq. (11.33), the relativistic $\beta\gamma$ of an ion is straightforwardly expressed in terms of $B(t)$ as

$$\beta\gamma = \left(\frac{Z}{A}\right)\left(\frac{e\rho}{mc}\right)B. \tag{12.27}$$

The revolution frequency, $f = c\beta/C_0$, is described by

$$f = \frac{c}{C_0}\sqrt{\frac{D}{1+D}}, \tag{12.28}$$

where

$$D \equiv (\beta\gamma)^2 = \left[\left(\frac{Z}{A}\right)\left(\frac{e\rho}{mc}\right)\right]^2 B^2(t).$$

Similarly, the achieved kinetic energy of the ion is represented by

$$T = Amc^2\left(\frac{1}{\sqrt{1-\beta^2}} - 1\right) = Amc^2\left(\frac{1}{\sqrt{1-\left(\frac{fC_0}{c}\right)^2}} - 1\right). \tag{12.29}$$

Since dB/dt is not constant for the rapid-cycle synchrotron, the accelerating voltage, $V_{acc}(t)$, must change in time. Due to the nature of the induction acceleration system of a 1-to-1 transformer, the output voltage at the induction cell is the same as the output voltage of the DC power supply energizing the switching power supply. Therefore, it is difficult in a practical sense to change the acceleration voltage within one acceleration period on the order of several tens of milliseconds. Fortunately, a demanded energy gain per unit time Δt, $\Delta E = ZeV_{acc}(t)f(t)\Delta t$, is provided with a constant accelerating voltage, V_0, and a modified switching frequency, $g(t) = V_{acc}(t)f(t)/V_0$. In other words, the pulse density for acceleration is controlled. Namely, the gate trigger signal is intermittently generated. Usually, multiple induction acceleration cells are ready for acceleration. It is also possible to control in real time the number of dedicated acceleration cells. A combination of these two ways will be employed to generate the required accelerating voltage described by Eq. (12.26).

12.4.4 Longitudinal Confinement

Here, it should be noted that the switching capability of the commercially available switching element is limited to 1 MHz operation because of heat deposited on the switching element, itself. In a later region of the acceleration period in the medium energy AIA, the revolution frequency will exceed 1 MHz, as shown in Fig. 12.22. Superimposing pulse voltages intermittently triggered is a realistic technique to overcome the limited rep-rate. For instance, every induction cell devoted to confinement is simultaneously triggered every three turns in the acceleration region with a revolution frequency of 3 MHz, as can be seen in a typical example. The ion beam receives a three times larger confinement voltage than the required one in the case that the induction cells are triggered every turn.

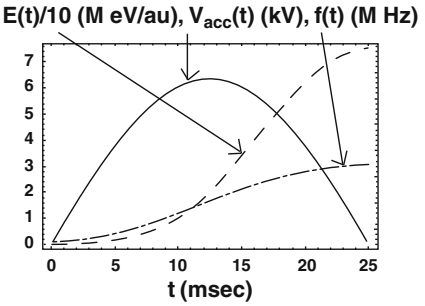

Fig. 12.22 Energy gain (*left*), required acceleration voltage (*middle*), and revolution frequency (*right*) versus time

12.4.5 Stacking and Beam Handling Through the Acceleration

A chopped ion beam is injected into the AIA in a single turn. The barrier step-voltages are excited to capture the chopped beam. From the practical limit of current

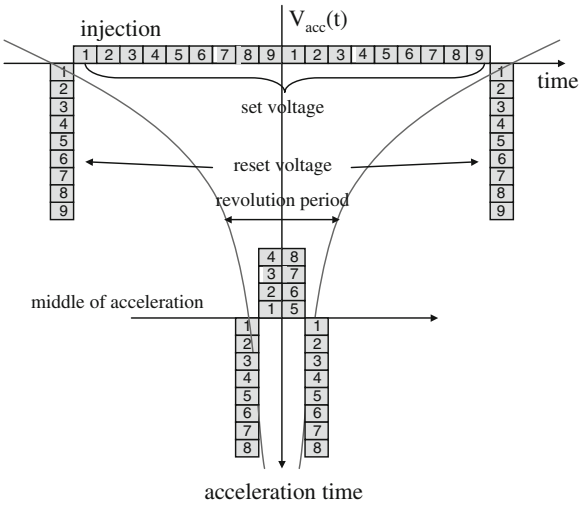

Fig. 12.23 Acceleration voltage pattern. The numbers are identification numbers of the induction acceleration cells. The set voltage is generated with an accompanying reset voltage within a single revolution period if the revolution period is larger than 1 μs. Otherwise, the acceleration cells are intermittently triggered

technology, the maximum pulse length for the induction acceleration voltage and its amplitude are of the order of 500 ns and 2 kV, respectively. The required long accelerating-voltage is generated by superimposing induction-voltage pulses with a finite pulse width, finite amplitude, and limited rep-rate, in time. Its scheme is shown in Fig. 12.23. Multiple acceleration cells driven by an individual switching power-supply entry from the beginning of acceleration and the super-imposed acceleration voltage-pulse length are shown, as well as the time-duration between the barrier voltage pulses. As the acceleration proceeds, the revolution period decreases. The entire acceleration process, which has been obtained by computer simulations [47, 48], is depicted in Fig. 12.24.

12.4.6 Transverse Focusing

Transverse focusing of an ion beam in a circular ring is also important. In a strong focusing lattice, the transverse motion of an ion is governed by the following equation:

$$Am\frac{\mathrm{d}}{\mathrm{d}t}(\gamma v_{\perp}) = -Zev_{\parallel}B'x, \tag{12.30}$$

where

$$B' \equiv \frac{\partial B_y}{\partial x}.$$

Using the orbit coordinates instead of the time-derivative, Eq. (12.30) takes the well-known form of the betatron equation. Assuming that the changes in γ and β per turn

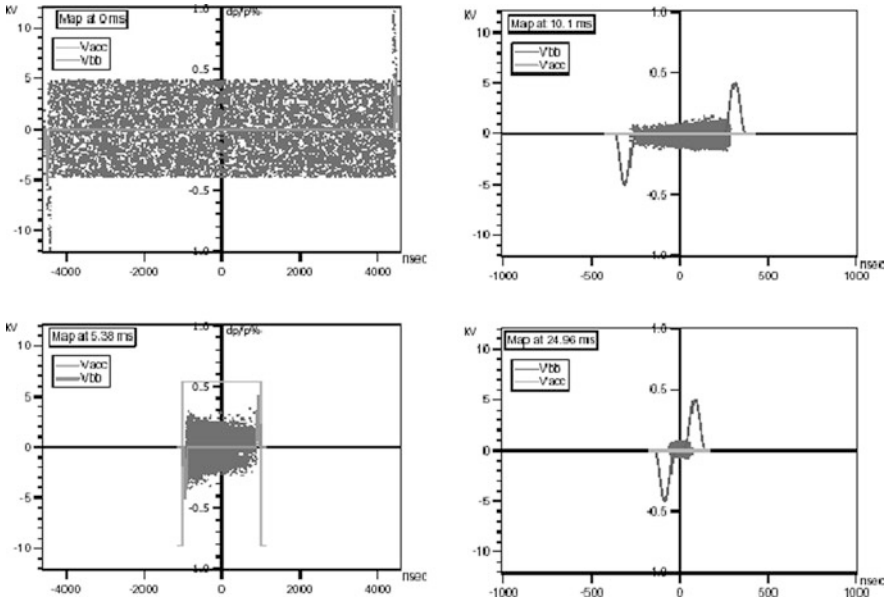

Fig. 12.24 Temporal evolution of an Ar^{18} bunch in the longitudinal phase-space. Phase plots from *left top* to *right bottom* show the ion bunch right after injection, at 5 ms, at 10 ms, and at the end of the acceleration, respectively. The output voltage (*gray*) is 1.08 kV for acceleration, and the integrated barrier voltage is 5 kV

are small, we have an approximated betatron equation,

$$\gamma_c \beta_\parallel \frac{\mathrm{d}}{\mathrm{d}s}\left(\frac{\mathrm{d}x}{\mathrm{d}s}\right) = -\frac{Z}{A}\left(\frac{e}{m}\right) B' x \Rightarrow \frac{\mathrm{d}^2 x}{\mathrm{d}s^2} + K(s)x = 0, \tag{12.31}$$

where

$$K(s) = \left(\frac{Z}{A}\right)\frac{e/m}{c\beta\gamma}\frac{\partial B_y}{\partial x}. \tag{12.32}$$

Substitution of Eq. (12.27) into Eq. (12.32) yields

$$K(s) = \frac{1}{B\rho}\frac{\partial B_y}{\partial x}. \tag{12.33}$$

The k-value does not depend on the ion mass or its charge state; the betatron tune for any ion or any charge state is always the same. Once any ion is injected into the AIA with an appropriate momentum, as discussed later, the transverse beam dynamics through the entire acceleration is common among all ions.

12.4.7 Space Charge Limited Ion-Beam Intensity

A number of ions subject to acceleration in the AIA are restricted by space-charge effects at injection because of an extremely low β. Its magnitude can be estimated by the term of the Laslett tune-shift,

$$\Delta\nu \propto \frac{Z^2 N}{B_f \beta^2 \gamma^3}, \tag{12.34}$$

where N is the number of charged particles per bunch and B_f is the bunching factor. It is assumed that the beam size is uniquely determined by an acceptance of the aperture. It is believed that $\Delta\nu$ is 0.25 in the space-charge limit. Thus, the allowed magnitude of N is known from Eq. (12.34). This number has been experimentally known for the proton in the KEK 500 MeV Booster.

The space-charge limited number of ions per bunch, N_i, is straightforwardly obtained using N_p, as shown in the following equation:

$$\frac{N_i}{N_p} = \left(\frac{A}{Z^2}\right)\left(\frac{\beta_i^2\gamma_i^3}{\beta_p^2\gamma_p^3}\right)\frac{(B_f)_{\mathrm{AIA}}}{(B_f)_{\mathrm{RF}}} \cong \frac{1}{Z}\frac{V_i}{V_p}\frac{(B_f)_{\mathrm{AIA}}}{(B_f)_{\mathrm{RF}}}, \tag{12.35}$$

where the under-suffices "p" and "i" denote the parameters for a proton and an ion, respectively. Here, $(B_f)_{\mathrm{AIA}}$ is a bunching factor in the all-ion accelerator, which has been estimated to be 0.7–0.8 from extensive simulation work as described in Sect. 11.2.1. From the long experience of the KEK Booster operation for protons in the space-charge limited operation mode, where the injection voltage is $V_p = 40$ MV, we know that $N_p = 3 \times 10^{12}$ and $(B_f)_{\mathrm{RF}} = 0.3$. Substituting these numerical parameters and the injection voltage, $V_i = 200$ kV, into Eq. (12.35), we can evaluate the expected space-charge limiting current for typical ions. For three cases of $^{12}C^{+6}$, $^{40}Ar^{+18}$, and $^{197}Au^{+79}$, we obtain $N_i = 6.5 \times 10^9$, 2.2×10^9, and 0.49×10^9 per bunch, or 6.5×10^{10}, 2.2×10^{10}, and 4.9×10^9 per second, respectively. For simplicity, the same transverse emittance as that of proton is assumed here.

The beam intensity suggested here is not very high but sufficiently attractive for material science. If the extracted ion beams are focused through a kind of mini-beta focusing system familiar in colliders, the beam size can be drastically reduced on a metal target, creating a higher intensity beam. Bunch rotation in the longitudinal phase-space is known to compress the ion bunch in time. Accordingly, a limited region in the 3D physical space, where an ion beam manipulated in such a way looses most of its kinetic energy, will serve for warm dense matter science [49].

12.4.8 Vacuum

Vacuum is the most important parameter because the survival rate of an ion beam depends on the loss due to electron capture or stripping. This loss originates

from electron capture or stripping as a result of the collision with residual gas molecules. Two processes will be fatal from the viewpoint of beam loss, although other processes, such as Möller scattering leading to emittance blow-up are likely to occur. The cross-sections of these physics process will strongly depend on the velocity of the ion beam and the achieved pressure. A simple estimation of beam intensity survival is described to help locate a requirement in the vacuum system design. Here, it should be noted that the Ar^{+Z} ions are assumed to exit the 200 kV high voltage terminal with an energy of $200(Z/A)$ keV/au, where $A = 40$. The probability of capturing one electron is given by the cross-section σ_c, and that of the loss of an electron by σ_l. These are governed by velocity dependencies of different types. A figure representing the following expression can be found from a private note by Jean-Michel Lagniel,

$$\sigma_c \propto Z^2\beta^{-5}, \qquad \sigma_l \propto Z^{-2}\beta^{-2} \tag{12.36}$$

Here, β indicates the relativistic beta. It is obviously practical and useful to use actual experimental results, where nitrogen is assumed as a residual gas. A major source of loss is known to be electron capture below a few MeV/au and stripping beyond that value. The survival ratio at time t from injection is given by

$$S = \frac{n(t)}{n(0)} = \exp\left[-2.12 \times 10^{27} P_{\text{torr}} \int_0^t \sigma_{\text{tot}}\beta \mathrm{d}t\right] \tag{12.37}$$

Here $\sigma_{\text{tot}} = \sigma_c + \sigma_l$ and β change with acceleration and are determined from the ramping pattern of the bending field. Substituting of $\sigma_c = \sigma_{c0}\left[\beta(0)/\beta(t)\right]^5$ and $\sigma_l = \sigma_{l0}\left[\beta(0)/\beta(t)\right]^2$, where σ_{c0} and σ_{l0} are derived from the experimental results obtained by I.S. Dmitriev et al. [50], into Eq. (12.37) shows that a vacuum of 10^{-7} P is required to achieve a survival rate of more than 90%. It is emphasized that the injector-free all-ion accelerator must be operated under a much better vacuum condition compared with the typical vacuum of 10^{-6} P in conventional heavy ion accelerators.

12.4.9 Ion Source and Injector

The injection energy is low and its magnitude depends on an extraction voltage from an ion source. Assuming a fixed injection field, its total acceleration voltage is adjusted to

$$V \cong \frac{1}{2}\left(\frac{Z}{A}\right)\left(\frac{e\rho^2 B^2}{m}\right) = \left(\frac{Z}{A}\right) V_{\text{inj}}^p, \tag{12.38}$$

where eV_{inj}^p is the injection energy of a proton into the AIA. Ion sources such as an electron cyclotron resonance ion source (ECRIS), electron beam ion source (EBIS),

or laser ablation ion source (LAIS) may be possible candidates. For the AIA, where fully stripped ions are required for the high acceleration efficiency and heavy metal ions including gas ions are requested for various applications, the LAIS appears to be particularly suitable, although there is still a technical problem, such as a frequent change of the target surface. So far, a broad spectrum of charge states including a high charge state for Iron and Carbon has been demonstrated by Okamura et al. [51].

12.4.10 Summary

Various heavy ions of medium-energy delivered from the AIA should be quite attractive in a wide scope of applications from warm dense matter science to medical science. If a short acceleration gap in the induction acceleration cell and good vacuum were to be realized, even cluster ions, such as albumin of $A = 5 \times 10^4$ and $Z < 50$, could be accelerated in the AIA [52]. A large dynamic range of the guiding magnetic fields in the AIA is required to achieve an attractive high energy far beyond that of the electrostatic accelerators. In order to satisfy this demand, the choice of high field superconducting magnets may be a possible solution. However, there are two significant shortcomings that the field uniformity in the low field region is largely affected by persistent currents and the superconducting magnet cannot be rapidly ramped nor demagnetized. It is only reported that the magnetic field ramp rate up to 4 T/s with the minimum/maximum magnetic flux density of 0.5/4.0 Tesla should be achievable [53]. These features do not allow us to employ the high field superconducting magnet for the rapid cycle AIA assuming its operation at more than 10 Hz. Thus, we arrive at a concept of induction sector cyclotron [54], where the required guiding fields are constantly excited and the dynamic range of guiding fields is traded off the rotation radius within the pole gap. The induction sector cyclotron may be an interesting alternative of the AIA.

References

1. S. Mishra. High Luminosity Operation of the Fermilab Accelerator Complex. In *Proceedings of the 2003 Particle Accelerator Conference*, pages 1–5, Portland, OR, 12–16 May 2004.
2. M. Harrison, S. Peggs, and T. Roser. The RHIC Accelerator. *Ann. Rev. Nuc. Part. Sci.*, 52: 425–469, 2002.
3. The Large Hadron Collider, Conceptual Design. Technical Report CERN Report CERN/AC/ 95-05 (LHC), CERN, 1995. edited by P. Lefevre and T. Petterson.
4. Y. Shimosaki, K. Takayama, and K. Torikai. Quasiadiabatic, Nonfocusing Transition-Energy Crossing. *Phys. Rev. Lett.*, 96:134801–134804, 2006.
5. E. Courant and H. Snyder. Theory of the Alternating Gradient Synchrotron. *Ann. Phys*, 3:1, 1958.
6. H. Antosiewicz. *Handbook of Mathematical Functions with Formulas, Graphs, and Mathematical Tables*, Dover, New York, NY, 1970.
7. K. Takayama, J. Kishiro, M. Sakuda, Y. Shimosaki, and M. Wake. Superbunch Hadron Colliders. *Phys. Rev. Lett.*, 88:144801–144804, 2002.

8. K. Takayama. Superbunch Hadron Colliders. In *Proceedings of the International Workshop on Recent Progress in Induction Accelerators*, pages 39–46, Tsukuba, Japan, 29–31 Oct. 2003. KEK.
9. O. Bruning, R. Cappi, R. Garoby, O. Grobner, W. Herr, T. Linnecar, R. Ostojic, K. Potter, L. Rossi, F. Ruggiero, K. Schindl, G. Stevenson, L. Tavian, T. Taylor, E. Tsesmelis, E. Weisse, and F. Zimmermann. LHC Luminosity and Energy Upgrade: A Feasibility Study. Technical Report CERN Report (LHC Project Report 626), CERN, 2002.
10. W. Fischer, M. Blaskiewicz, and J. Wei. Possible RHIC Upgrades with Superbunches. In *Proceedings of the International Workshop on Recent Progress in Induction Accelerators*, pages 5–10, Tsukuba, Japan, 7–10 Mar. 2007. KEK.
11. H. Glass, G. Foster, P. Limon, E. Malamud, P. Garbincius, S. Peggs, J. Straight, M. Syphers, J. Tompkins, and A. Zlobin. Design Study for a Staged Very Large Hadron Collider. Technical Report FNAL Report Fermilab-TM-2149, FNAL, 2001.
12. K. Johnsen. CERN Intersecting Storage Rings. *Nucl. Inst. Meth.*, 108:205–223, 1973.
13. K. Johnsen. The ISR and Accelerator Physics, Part I in A Review of Accelerator and Particle Physics at the CERN Intersecting Storage Rings. Technical Report CERN Report (CERN 84-13), CERN, 1983.
14. E. Keil. Luminosity Optimisation for Storage Rings with Low-β Sections and Small Crossing Angles. *Nucl. Inst. Meth.*, 113:333–339, 1973.
15. H. Hahn, M. Month, and R. Rau. Proton–proton Intersecting Storage Accelerator Facility ISABELLE at the Brookhaven National Laboratory. *Rev. Mod. Phys.*, 49:625–679, 1977.
16. J. Sanford and D. Matthews. Site-Specific Conceptual Design of the Superconducting Super Collider. Technical Report SSC Report (SSC-SR-2020, DE93 007234), SSC, 1990.
17. Y. Shimosaki. Crossing Geometry and Beam–Beam Tune Shift in a Superbunch Hadron Collider. Technical Report KEK-Report 2004-7, KEK, 2004.
18. F. Ruggiero, G. Rumolo, F. Zimmermann, and Y. Papaphilippou. Beam Dynamics Studies for Uniform (Hollow) Bunches or Super-bunchesin the LHC: Beam–Beam Effects, Electron Cloud, Longitudinal Dynamics, and Intra-beam Scattering. In *Proceedings of the International Workshop on Recent Progress in Induction Accelerators*, pages 131–147, Tsukuba, Japan, 29–31 Oct. 2003. KEK.
19. H. Grote. Beam–beam effects in the LHC. In *Proceedings of the Workshop on Beam–Beam Effects in Large Hadron Colliders*, pages 59–62, Geneva, Switzerland, 12–17 Apr. 1999. CERN. (CERN Report CERN-SL-99-039 AP).
20. Y. Shimosaki and K. Takayama, Beam–Beam Effects in Superbunch Collision: Weak–Strong Model, Snowmass 2001, M401 (unpublished).
21. Y. Shimosaki. Beam–Beam Effects in the Inclined Super-Bunch Crossing. In *Proceedings of the International Workshop on Recent Progress in Induction Accelerators*, pages 126–130, Tsukuba, Japan, 29–31 Oct. 2003. KEK.
22. W. Herr and J. Miles. Optimizing the LHC Interaction Region to Obtain the Highest Possible Luminosity. In *Proceedings of the 1996 European Particle Accelerator Conference*, pages 424–426, Sitges, Spain, 10–14 June 1996.
23. W. Chao. *Physics of Collective Beam Instabilities in High Energy Accelerators*, Wiley, New York, NY, 1993.
24. T. Toyama and K. Takayama. Collective Instability of a Super-Bunch. In *Proceedings of the International Workshop on Recent Progress in Induction Accelerators*, pages 148–151, Tsukuba, Japan, 29–31 Oct. 2003. KEK.
25. Y. Shimosaki, T. Toyama, and K. Takayama. Head–Tail Instability of a Super-bunch. In *Proceedings of 33rd ICFA Advanced Beam Dynamics Workshop on High Intensity and High Brightness Hadron Beams, AIP Conference Proceedings No. 773*, pages 304–306, Bensheim, Germany, 18–22 Oct. 2005. GSI.
26. G. Rumolo. Intensity Limitations by Combined and/or (Un)Conventional Impedance Sources. In *Proceedings of HHH-2004: First CARE-HHH-APD Workshop on Beam Dynamics in Future Hadron Colliders and Rapidly Cycling High-Intensity Synchrotrons, CERN-2005-006*, pages 249–259, Geneva, Switzerland, 8–10 Nov. 2005. CERN.

27. R. Macek. Overview of New Developments on the PSR Instability. In K. Hackay and R. Macek, editors, *Proceedings of Workshop on Two-Stream Instabilities in Accelerators and Storage Rings*, Santa Fe, NM, 16–18 Feb. 2000. ANL and LANL.
28. J. Wei. Synchrotrons and Accumulators for High-Intensity Proton Beams. *Rev. Mod. Phys.*, 75:1383, 2003.
29. J. Jimenetz, G. Arduini, P. Collier, G. Ferioli, B. Henrist, N. Hilleret, L. Jensen, K. Weiss, and F. Zimmermann. Electron Cloud with LHC-Type Beams in the SPS: A Review of Three Years of Measurements. In *Proceedings of ECLOUD 02, Geneva, CERN-2002-001*, pages 17–28, Geneva, Switzerland, 15–18 Apr. 2002. CERN.
30. V. Danilov, A. Aleksandrov, J. Galambos, D. Jeon, J. Holmes, and D. Olsen. Multipacting on the Trailing Edge of Proton Beam Bunches in the PSR and SNS. In *Proceedings of Workshop on Instabilities of High-Intensity Hadron Beams in Rings, AIP Conference Proceedings No. 496*, pages 315–320, New York, NY, 28 June–1 July 1999. Brookhaven National Laboratory.
31. A. Piwinski. Intrabeam Scattering. In *Proceedings of the 9th International Conference on High Energy Accelerators*, pages 405–409, Stanford, CA, 2–7 May 1974. SLAC.
32. J. Bjorken and S. Mtingwa. Intrabeam Scattering. *Part. Accel.*, 13:115–143, 1983.
33. A. Piwinski. CAS CERN Accelerator School Advanced Accelerator Physics. Number CERN-Report 87-03, pages 402–415, 1987.
34. D. Neuffer and S. Peggs. Beam-Beam Tune Shifts and Spreads in the SSC (Superconducting Super Collider): Head On, Long Range, and Pacman Conditions. Technical Report SSC Report SSC-63, SSC, 1986.
35. E. Lawrence and M. Livingston. The Production of High Speed Protons Without the Use of High Voltages. *Phys. Rev.*, 38:834, 1931.
36. M. White, M. Isaila, K. Prelec, and H. Allen. Acceleration of Nitrogen Ions to 7.4 Gev in the Princeton Particle Accelerator. *Science*, 174:1121–1123, 1971.
37. J. Alonso, R. Avery, T. Elioff, R. Force, H. Grunder, H. Lancaster, E. Lofgren, J. Meneghetti, F. Selph, R. Stevenson, and R. Yourd. Acceleration of Uranium at the Bevalac. *Science*, 217:1135–1137, 1982.
38. Y. Hirao, H. Ogawa, S. Yamada, Y. Sato, T. Yamada, K. Sato, A. Itano, M. Kanazawa, K. Noda, K. Kawachi, M. Endo, T. Kanai, T. Kohno, M. Sudou, S. Minohara, A. Kitagawa, F. Soga, E. Takada, S. Watanabe, K. Endo, M. Kumada, and S. Matsumoto. Heavy ion synchrotron for medical use HIMAC project at NIRS-Japan. *Nucl. Phys. A*, 538:541–550, 1992.
39. P. Spiller. Challenges and Progress in the Fair Accelerator Project. In *Proceedings of the 2005 Particle Accelerator Conference*, pages 294–298, Knoxville, TN, 16–20 May 2005.
40. M. Odera, Y. Chiba, T. Tonuma, M. Hemmi, Y. Miyazawa, T. Inoue, K. Kambara, M. Kase, T. Kubo, and F. Yoshida. Variable Frequency Heavy-ion Linac, RILAC:I. Design, Construction and Operation of Its Accelerating Structure. *Nucl. Inst. Meth. A*, 227:187–195, 1984.
41. A. Ruggiero. RF Acceleration with Harmonic Number Jump. *Phys. Rev. Special Topics – Accelerators and Beams*, 9:100101–100105, 2006.
42. K. Takayama, Y. Arakida, T. Iwashita, Y. Shimosaki, T. Dixit, and K. Torikai. All-Ion Accelerators: An Injector-Free Synchrotron. *J. Appl. Phys.*, 101:063304–063307, 2007.
43. K. Takayama, K. Torikai, Y. Shimosaki, and Y. Arakida, Patent No. 3896420, PCT/JP2006/308502(2006).
44. A. Weidinger. Ion Tracks – A New Route to Nanotechnology. *Europhys. News*, 35:152–155, 2004.
45. U. Glasmacher, M. Lang, H. Keppler, F. Langenhorst, R. Neumann, D. Schardt, C. Trautmann, and G. Wagner. Phase Transitions in Solids Stimulated by Simultaneous Exposure to High Pressure and Relativistic Heavy Ions. *Phys. Rev. Lett.*, 96:195701–195704, 2006.
46. National Task Force on High Energy Density Physics. Frontiers for Discovery in High Energy Density Physics. Office of Science and Technology Policy, National Science and Technology Council Interagency Working Group on the Physics of the Universe, 2004.
47. T. Dixit, T. Iwashita, and K. Takayama. Induction Acceleration Scenario from an Extremely Low Energy in the KEK All-Ion Accelerator. *Nucl. Inst. Meth. A*, 602:326–336, 2009.

48. T. Dixit, T. Iwashita, Y. Arakida, and K. Takayama. Digital Acceleration Scheme of the KEK All-Ion Accelerator. In *Proceedings of the 2008 European Particle Accelerator Conference*, pages 2797–2799, Genova, Italy, 23–27 June 2008.
49. T. Kikuchi, S. Kawata, and K. Takayama. Half-Mini Beta Optics with a Bunch Rotation for Warm Dense Matter Science Facility in KEK. In *Proceedings of the 2007 Particle Accelerator Conference*, pages 1541–1543, Albuquerque, 25–29 June 2007.
50. I.S. Dmitriev, Ya.A. Teplova, Yu.A. Belkova, N.V. Novikov, Yu.A. Fainberg. Experimental Electron Loss and Capture Cross Sections in Ion-Atom Collisions. *Atom. Data Nucl. Data Tables*, 96(1), 85–121, January 2010.
51. S. Kondrashev, T. Kaneue, M. Okamura, and K. Sakakibara. Features of Ion Generation Using Nd-Glass Laser. *J. Appl. Phys.*, 100:103301–103308, 2006.
52. Y. Oguri, J. Hasegawa, M. Ogawa, K. Horioka, and K. Takayama. Beam-Plasma Interaction Experiments at PLNR and Possible Applications of Induction Synchrotrons. In *Proceedings of the International Workshop on Recent Progress in Induction Accelerators*, pages 139–145, Tsukuba, Japan, 7–10 Mar. 2006. KEK.
53. P. G. Akishin, A. V. Butenko, A. D. Kovalenko, and V. A. Mikhaylov. Field Study of the 4 T Superconducting Magnet for Rapid Cycling Heavy Ion Synchrotrons. In *Proceedings of the 2004 European Particle Accelerator Conference*, pages 1390–1392, Lucerne, Switzerland, 5–9 July 2004.
54. K. Takayama, PATENT pending Nov. 2009.